Department of Precision and Microsystems Engineering

Designing a Suspended Silicon Nitride GHz Acoustic Beam Splitter

Maximiliaan van der Vis

Report no : 2023.002
Coaches : Dr. G.J. Verbiest and Dr. R.A. Norte
Specialisation : ED
Type of report : MSc Thesis
Date : 19-01-2023

Designing a Suspended Silicon Nitride GHz Acoustic Beam Splitter

by

Maximiliaan van der Vis

Student number:	4474716
Thesis committee:	Dr. G.J. Verbiest
	Dr. R.A. Norte
	Dr. A.M. Aragon

Abstract

Research has shown concepts of phononic integrated circuits (PnICs) consisting of multiple acoustic waveguides and beam splitters. Traveling acoustic waves experience energy loss when moving. Minimizing these losses is critical for large and complex PnICs. By fabricating on-chip PnICs, it is possible to operate under vacuum and at low temperatures resulting in lower acoustic losses.

Studies have shown on-chip data transport using straight acoustic waveguides fabricated inside suspended membrane phononic crystals. The use of high stress Silicon Nitride (SiN) has enabled the manufacturing of high aspect ratio suspended structures. This is achieved by stress keeping the membrane under tension resulting in a flat surface.

Current acoustic beam splitter designs feature liquid and air for the wave supporting material. Making them not suitable for on-chip devices. Therefore, on-chip PnICs require a new type of splitter design.

In this study, finite element methods are used to investigate if suspended SiN membranes offer a solution for on-chip acoustic beam splitting. The wave confinement of square and hexagonal lattice splitters are also compared to find the best performing design. Phononic bandstructures are constructed by performing eigenfrequency studies on various 2D phononic crystal unit cells. These bandstructures reach full GHz bandgaps with relative bandgap sizes of 57.3%.

Symmetric beam splitters are then made by introducing line defects into the crystal structures. Multiple wave excitation locations, frequencies and waveguide widths are investigated to establish the highest wave confining splitter design. The final design consists of a y-shaped splitter inside a suspended SiN hexagonal lattice phononic crystal and achieves a wave confinement of 85.03% at an excitation frequency of $3.25GHz$.

The results show that suspended SiN membranes featuring hexagonal lattice phononic crystals offer a promising solution for on-chip beam splitting.

Contents

1 Introduction

When thinking of data or energy transmission, light waves and electrons are some of the first things that come to mind. Recently, a rather unexplored field has gathered more interest for research. Engineered devices that control mechanical vibrations or acoustic waves that interact with phononic crystals (PnCs). These devices offer solutions that their electromagnetic counterparts are less or not suited for. The ability of acoustics to couple to any system makes connections between different systems easier [13]. This makes acoustics important for all technology fields in the classical and quantum regimes.

Quantum research has shown valuable use of phonons, the quanta of mechanical vibrations. Due to their typical frequency range, they behave well as a bridge between the classical and quantum regimes [33] [11]. Another possibility of phonons is that the tuning and guiding of acoustic waves is useful for heat transport control [47] [44] and that acoustics can be used to scan through opaque materials [38]. Finally, the rising demand for data transfer and storage causes its energy consumption to reach unsustainable heights. The use of phonons for data carrying is currently being researched as a low-energy carrier alternative to overcome this issue [39]. Projects such as the Horizon 2020 Phenomen are funded by the EU to help support the early stages of this technology [37].

Fu et al. (2019) [9] presented an experimental on-chip phononic integrated circuit (PnIC) showing the need to be able to split acoustic waveguides (WGs) into multiple directions. On-chip beam splitters have numerous advantages over conventional devices. By having on-chip structures, it is possible to operate under vacuum and cryogenic temperatures. This results in minimal losses needed for large complex acoustic systems containing multiple WGs and beam splitters. Furthermore, these on-chip splitters will enable direct signal processing, routing, filtering, demultiplexing and sensing [2].

In photonics, the study and application of photons, there are multiple ways to achieve splitters. Even simply letting the optical WG split symmetrically has been shown to work [26] [5].

Acoustic research also shows WGs and possibilities for wave splitting. However, there have been no on-chip acoustic beam splitters shown to work.

Several studies involving suspended PnC structures show these acoustic waveguides can transmit mechanical vibrations across a chip. With demonstrations of MHz out-of-plane vibrations [23] [45] done at room temperature with the use of high stress ($1GPa$) Silicon Nitride (SiN) [30]. GHz wave confinement is shown for in-plane vibrations at cryogenic [35] and room temperature operations [28].

Acoustic beam splitters have been researched in two main ways. The first is by using cone-like structures where the reflectivity can be altered by line defects in square crystal lattices. Numerical studies involving up to GHz vibrations show methods for altering the reflection and transmission ratios of the incident waves by adjusting the radii of the cylinders in the line defects [19] [27] [49]. The second way is to introduce multiple direction waveguides inside the crystal structure. Wave splitting of kHz frequencies is demonstrated by introducing 90° bends inside line defects [46] and y-shaped waveguides [41] inside square lattice structures.

Most of the splitter studies consist of solid-to-liquid or liquid-to-liquid interfaces with the acoustic wave traveling in the liquid material. These types of designs are not achievable in on-chip devices and thus a new type of splitter design is needed.

It is also noticed that no studies involve GHz out-of-plane vibrations at room temperature. What makes out-of-plane vibrations interesting, is that they can be measured using pulsed lasers. This reduces fabrication complexity since there is no need to add other on-chip structures for wave detection. GHz frequencies also reduce device sizes due to a shorter wavelength compared to lower frequency vibrations.

Research shows a decrease in material damping (intrinsic losses) at cryogenic temperatures [25] [36]. However, these low temperatures make device integration more difficult compared to devices that operate at room temperature. Designing a device for room temperature operation ensured its functioning in the most challenging environment. When lower losses are needed the operating temperature can then be lowered.

Suspended structures made of high stress SiN have lower material and environmental damping losses. Stress increases the elastic energy storage inside a material, lowering the intrinsic losses. However, for GHz frequencies the deformations are small. This reduces the impact of the increased elastic energy storage. The high stress also helps with the manufacturing of high aspect ratio structures. This is therefore the main reason to use high stress materials in GHz applications.

Furthermore, most splitter designs feature square crystal lattices. For symmetric splitting of acoustic waves, a y-shaped hexagonal lattice splitter has $60°$ splitting angles whereas square lattices result in $90°$ splitting angles. Using hexagonal lattices can decrease the reflection of the incident wave at the splitter location, lowering the energy losses caused by the splitter. A hexagonal lattice would also maintain the waveguide geometry after the splitter which is not possible for a y-shaped splitter in a square lattice.

In this study, two research questions are investigated. First, could suspended SiN membranes offer the solution for on-chip GHz out-of-plane acoustic beam splitters operating at room temperature? Second, do hexagonal lattice splitters result in higher wave confinement compared to square lattice splitters?

To answer these questions, designs for suspended SiN GHz acoustic beam splitters operating under vacuum at room temperature are made and studied. The wave confinement of the different designs is compared to find the highest confining splitter design. This is done with the use of the FEM solver COMSOL Multiphysics in combination with the computing platform MATLAB.

The study starts with a technical background in PnCs, suspended membranes, elastic waves and pulsed lasers. Then the current state of the art regarding acoustic beam splitters and suspended PnC waveguides is given. Chapter 3 will show the used method for designing suspended acoustic beam splitters. Starting with fabricating hexagonal and square crystal lattice bandstructures that possess full bandgaps. Then, different techniques for coupling wave excitation to waveguides and influences of excitation frequencies are studied. Next, hexagonal and square lattice splitters are designed and their wave confinements are compared.

Finally, the splitter design that achieves the highest wave confinement is given. This is followed up by discussing the results and possible recommendations for future work.

2
Technical Background

This chapter consists of an overview of the different techniques and physics used in this study. It starts by explaining acoustic waves in solids. Second, suspended membranes are discussed and their fabrication is explained. Then, phononic crystals are introduced together with the workings of their bandstructures. Following are the methods for phonon generation and detection. Electrostatic forces, photothermal excitation and laser detection are explained. Then, the simulation of elastic waves is discussed. The next two sections give an overview of the current state-of-the-art regarding suspended membrane waveguides, acoustic wave guiding and beam splitters. Finally, a proposal for a phononic integrated circuit is shown.

2.1. Surface and Bulk acoustic waves

Traveling acoustic waves in solids are categorized into two main groups. Surface acoustic waves (SAW) and Bulk acoustic waves (BAW).

SAW, also known as Rayleigh waves, are waves that travel along the surface of a material. SAW can also exhibit different modes. Rayleigh-like modes, where the surface is moved in an elliptical manner, and love-like modes, where the surface is moved side to side perpendicular to the propagation direction. Love-like surface modes travel the fastest and for both modes, their amplitudes decrease exponentially with depth.

BAW travel in the interior of the medium. Just like SAW, BAW also exhibit different modes. Based on the displacement direction, known as polarization, the wave is either compressional (p-wave) or shear (s-wave). For P-waves, the polarization is parallel to the propagation direction. For S-waves, the polarization is perpendicular to the propagation direction. [12]. In figure 2.1 a visual representation of SAW and BAW are shown.

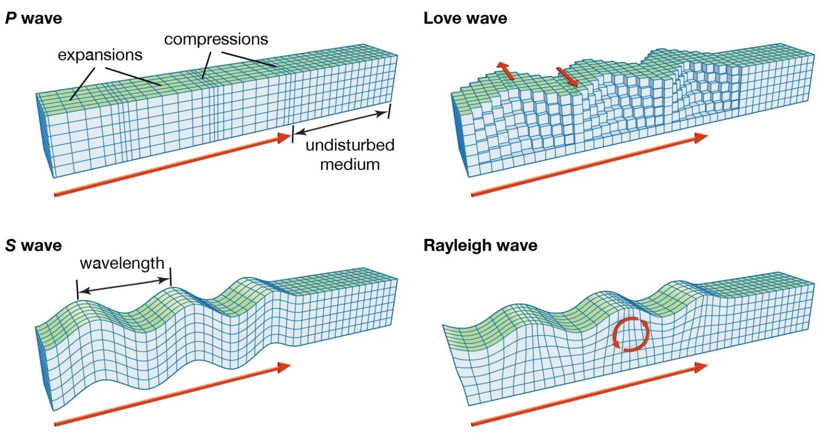

Figure 2.1: SAW and BAW wave types. (Encyclopaedia Britannica [6])

2.2. Suspended Membranes

Resonators and PnCs are often made from suspended membranes. An important reason for making a suspended structure is to lower its losses to the surrounding environment. In the case of phononics, it is to lower its acoustic loss. This is beneficial since this means the resonators have lower energy losses resulting in lower damping of their oscillations. This damping characteristic is described by the Q value. A higher Q value indicates a lower damping loss of the system. One of the most used techniques to fabricate thin film membranes is low-pressure chemical vapor deposition (LPCVD). In figure 2.2 the fabrication process of a suspended SiN membrane using LPCVD is shown. The LPCVD process is done in a high-temperature furnace. The first step is to deposit a thin layer of SiN on top of a solid substrate, in this case Silicon (Si). When the desired temperature is reached a source gas containing the wanted deposition chemicals is continuously run by the heated substrate. When the chemicals come into contact with the substrate surface they react and adhere to it, creating an even coating over the substrate. The second step involves a spin deposition technique where the substrate is spun whilst a photoresist material is deposited on top, again creating an even layer. Using lithography techniques, a mask can be made in the photoresist. Next, the pattern is transferred to the SiN with a plasma etch. After this, the mask is removed and the membrane is released from the substrate using a dry etch [42]

Because of the different thermal expansion coefficients of the Si substrate and the SiN membrane, a high residual stress of around $1GPa$ will be left inside the SiN membrane after fabrication. Stress increases the elastic energy storage inside a material, lowering the intrinsic losses. This enables higher Q values, meaning that less vibrational damping occurs [7]. These characteristics are beneficial for out-of-plane vibrations at room temperature.

The high stress also enables the fabrication of high aspect ratio structures. For membranes this means large surface area's with a small thickness. The high stress keeps the suspended structure taut (under tension), resulting in a flat membrane. In the case of GHz vibrations, the deformations are small causing a lower benefit of the increased elastic storage compared to kHz or MHz vibrations. The main reason to use high stress SiN with GHz applications is the possibility to manufacture high aspect ratio devices.

This high stress results in a critical membrane thickness of $250nm$. Membranes that exceed this limit have can form cracks. A thickness of $30nm$ is often used as the minimum thickness.[31]

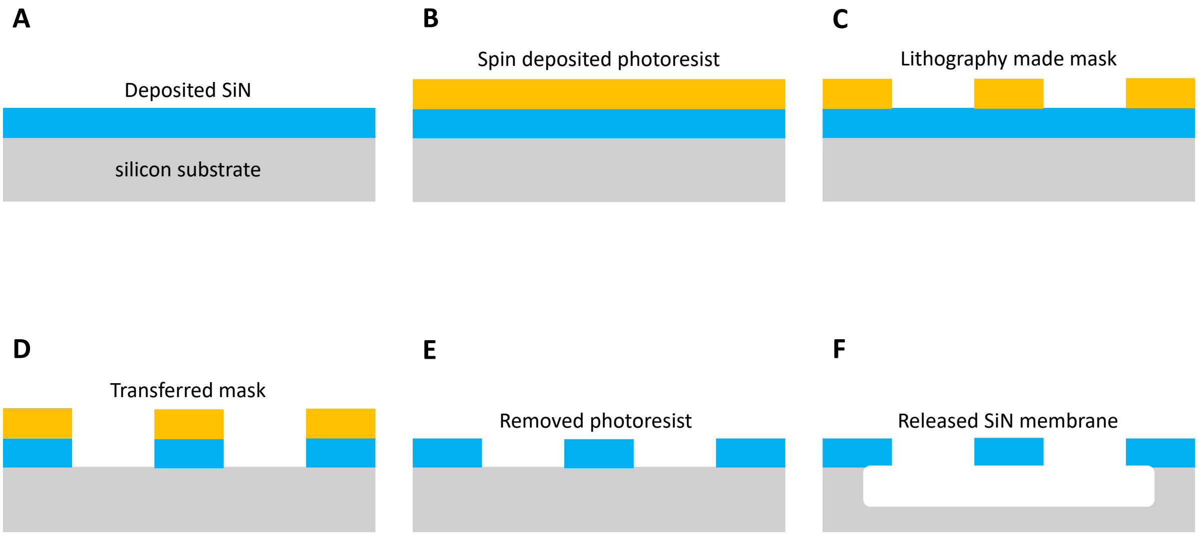

Figure 2.2: Schematic representation of a suspended membrane fabrication process. (a) SiN deposition on the Si substrate. (b) Photoresist spin deposition. (c) Lithograpy mask is made in the photoresist. (d) Plasma dry etch mask transfer. (e) Removal of the photoresist. (f) SiN released from the substrate creating the suspended membrane.

2.3. Phononic Crystals and Bandgap's

Materials that have engineered properties that are not found in naturally existing materials are called metamaterials. They are fabricated in periodic or non-periodic arrays of unit cells (the simplest repeating unit of the crystal). The periodic structure of the unit cells is known as the crystal lattice structure. An important dimension of the crystal lattice is the lattice constant, this is the length of the unit cell edge.[4]

Acoustic structures where periodically arranged unit cells cause periodic changes in reflection indexes, affecting the propagation of incident acoustic waves, are called phononic crystals (PnCs). The unit cells consist of rapid transitions of big and small masses, where the transition regions cause the change in reflection index. If this structure prevents the propagation of acoustic waves, meaning the transmission goes to zero caused by these periodic reflection indexes, it is known as a phononic shield. Figure 2.3 shows a simple representation of a phononic crystal with transitions of big and small masses.

Figure 2.3: Structure consisting of big (M) and small (m) masses.

PnCs inherit a characteristic bandstructure that is used to study their interactions with certain frequencies. It is possible for a bandstructure to have bandgaps. These are regions where the PnC behaves as a phononic shield. By altering the material properties like density, elasticity, geometry and periodicity of the unit cells, it is possible to design the bandgap around preferred frequencies or increase the bandgap size. In figure 2.4 an example of a PnC unit cell and its bandstructure is shown.

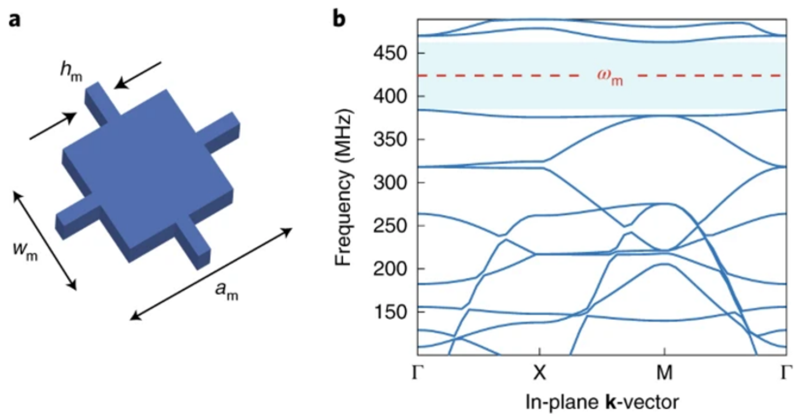

Figure 2.4: Example of a PnC unit cell with its band structure. (a) Unit cell of the PnC. (b) Band structure showing a complete bandgap in the blue shaded area. (Kalee et al. 2019 [18])

By adding defects into the crystal's periodicity, localized bandstructures are made. A defect that is enclosed by a crystal structure is called a cavity defect. The cavity can consist of a single spot defect or a line defect resulting from multiple defects along a specific direction. The defects are made by either removing, resizing or changing the orientation of the unit cells. Spot cavity defects are used to create asymmetric mode coupling, resulting in transmission strength depending on the incident wave direction. Line defects are used for guiding acoustic waves along a path that enables propagation inside the PnC. When a line defect is used to guide waves through a PnC it is called a waveguide (WG). Figure 2.5 shows some examples of defects in a square lattice.

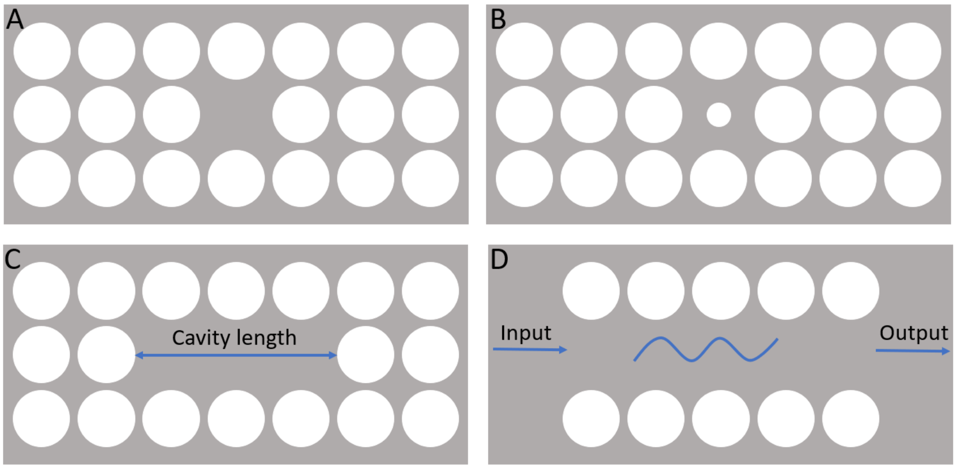

Figure 2.5: Examples of defects in a square crystal lattice. (a) Spot cavity defect formed by a removed circle (b) Spot cavity defect formed by adjusting the radius of a single circle (c) Line cavity defect (d) Line defect creating a waveguide through the crystal structure.

There are two main types of crystal lattice structures, square and hexagonal (triangular). The square lattice has four symmetry axis whereas the hexagonal lattice has six symmetry axis, as seen in figure 2.6 together with their respective irreducible Brillouin zones (IBZs). The IBZ represents the smallest symmetric part of the unit cell.

With suspended membrane PnCs, the lattice is fabricated by introducing holes inside the membrane. The geometry of these holes contributes to the determined bandgap of the PnC. The hole geometries can either be simple like square or circular or have more complex hole shapes like cross or shamrock style [8]. It is also possible to have a hybrid Lattice consisting of multiple style holes [1]. In figure 2.7 some examples of different unit cell types are shown.

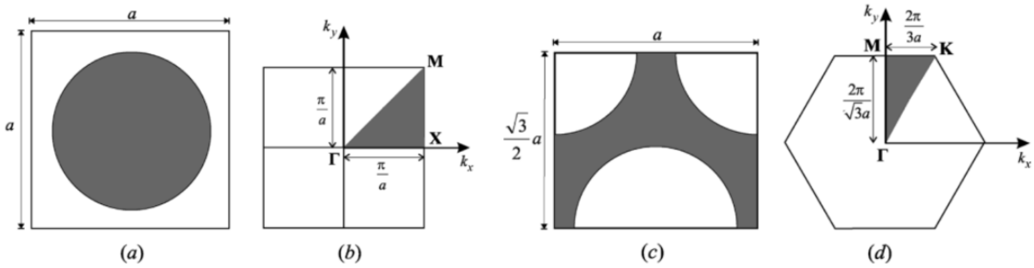

Figure 2.6: (a) Square lattice unit cell circular hole. (b) Square lattice IBZ. (c) Hexagonal lattice unit cell circular hole. (d) Hexagonal lattice IBZ. (Kosmidou et al. 2005 [22])

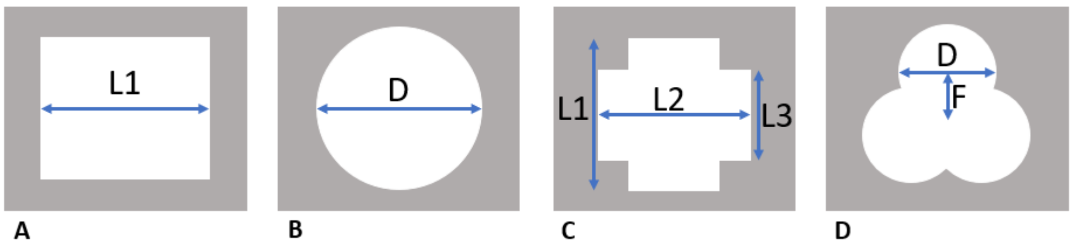

Figure 2.7: Unit cells of PnCs with (a) square hole, (b) circular, (c) cross and (d) shamrock shaped holes

The performance of a PnC is defined by its bandgap and the corresponding mid-gap frequency. The relative bandwidth (BG%) is used as a normalized performance metric of the PnC. Here, the absolute bandwidth is divided by the mid-gap frequency. This is important since this will take into account the wavelength ratio (lattice constant divided by the wavelength associated with the mid-gap frequency). A smaller wavelength ratio makes it easier to construct full bandgaps [10]. Because it effectively means having a higher concentration of unit cells per wavelength contributing to the wave guiding. A visualisation of the wavelength ratio is shown in figure 2.8.

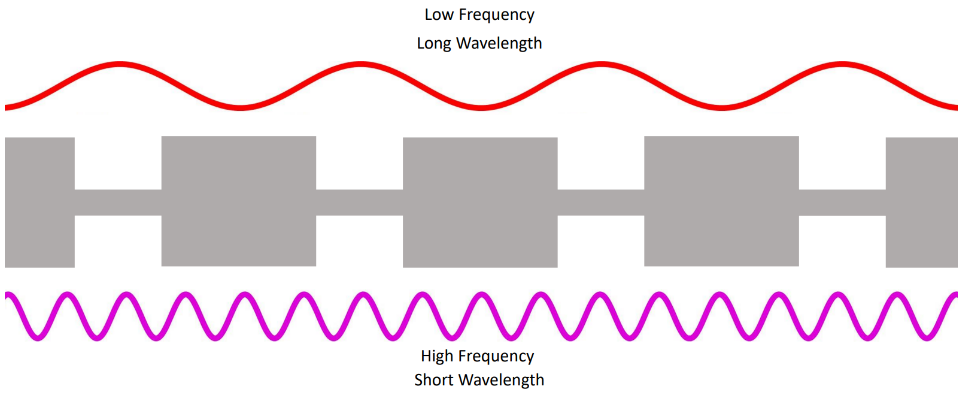

Figure 2.8: Visualisation of the wavelength ratio. The low frequency wave has a concentration of around one unit cell per wavelength. The high frequency wave has a lower concentration of unit cells per wavelength. Caused by the shorter wavelength.

It is found that for lattices with circular holes the BG% is dependent on the ratio of a/R. Where a is the lattice constant and R is the hole radius. With a higher BG% for a higher a/R ratio. Equation (2.1) shows the bandwidth equation and equation (2.2) shows the mid-frequency equation. Where, f_{top} is the upper and f_{bottom} is the lower bandgap frequency limit. Resulting from this, equation (2.3) describes the BG%. [16] [48]

$$\Delta f = f_{top} - f_{bottom} \tag{2.1}$$

$$f_{mid} = \frac{(f_{top} + f_{bottom})}{2} \tag{2.2}$$

$$BG\% = \frac{\Delta f}{f_{mid}} \tag{2.3}$$

2.4. Phonon Excitation and Detection

For the excitation of phonons, there are two main techniques. Either via electrostatic forces or with the use of photothermal excitation from photons. In this section, both working principles are explained.

2.4.1. Electrostatic Excitation

Coulomb's law, seen in equation (2.4), describes the force between two stationary charged particles. This force is called the electrostatic force. Where, K is coulombs constant ($K = 8.988 \times 10^9$ N·m^2 · C^{-2}), q_1 and q_2 are the charges of particles one and two respectively and r is the distance between the particles. To generate phonons using this force, there need to be two electrodes present. One on-chip and one probe electrode, seen in figure 2.9. By having an AC probe driven at a certain frequency, the electrostatic force between the electrodes will oscillate. Making them attract and repel each other, creating the wanted vibrations. It should be noted that in reality, this effect is only efficient for piezoelectric materials. These materials exhibit the so-called piezoelectric effect. Where electric polarization caused by mechanical strain is known as the direct piezoelectric effect and mechanical strain induced by an electric field is called the inverse piezoelectric effect. [3]

$$F = K\frac{|q_1 \times q_2|}{r^2} \tag{2.4}$$

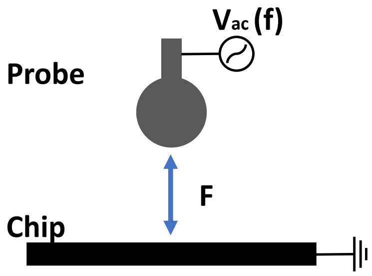

Figure 2.9: Electrostatic force between a probe and on-chip electrode. The AC driven probe creates attracting or repelling forces between the two electrodes.

2.4.2. Photothermal Excitation

Photons have momentum despite lacking mass. When photons have an impact this momentum energy is transferred as mechanical pressure onto the object. This force is called radiation pressure.

In equation (2.5) two relations of Photon energy (E) can be seen. Where, h is Planck's constant ($h = 6.62607015 \times 10^{-34}$ m^{2}kgs^{-1}), f is frequency (Hz), p is photon momentum and c is the speed of light. From the equation, it is seen that an increase in frequency will increase the energy. In other words, a longer wavelength decreases the photon energy. When light is absorbed by a material, it excited the electrons inside this material. The electrons will then interact with the nuclei of the material. This causes scattering, the forced deflection of a particle's traveling path, among the electrons that result in mechanical lattice waves (phonons). The increase in mechanical vibrations inside the material will effectively heat the material.

In reality, the lasers used in this study have a negligible radiation pressure force compared to the material expansion force caused by the absorbed light heating the material. A single light pulse creates around $66 * 10^{-12} N$ of radiation pressure and $3.75 * 10^{-7} N$ of expansion force. See appendix A for the calculations.

$$E = hf = pc \tag{2.5}$$

By using a pulsed laser there will be a range of excitation frequencies. The resulting acoustic wave pulse in the membrane is a Gaussian sine pulse, seen in equation (2.6). Here, A is the amplitude, μ is the expected value or pulse location, σ^2 is the variance or pulse width, and f_0 is the oscillation frequency. The exponential part represents the Gaussian distribution and the sinusoidal side is the wave pulse.

$$v(t) = A * exp(-\frac{(t-\mu)^2}{2\sigma^2}) * sin(2\pi f_0 t) \tag{2.6}$$

The Gaussian sine pulse is an oscillating sine with a varying amplitude A in the time domain. By analysing the frequency domain, a description of the time domain wave is made in terms of its frequency components and their specific magnitudes. Thereby finding the range of frequencies that the Gaussian sine pulse is constructed of. This is important because frequencies that lie outside the bandgap will affect the wave confinement. By using the Fourier transform, it is possible to go from the time domain to the frequency domain.

Table 2.1 shows the time and frequency domain functions of the exponential and sinusoidal part of the Gaussian pulse [29]. It is shown that the Gaussian distribution function is its own transfer function for $Re(\alpha) > 0$. When a function is multiplied by a sine, it is noted that the transform will consist of two identical peaks on either side of a center frequency. Figure 2.10 shows the transform results of a Gaussian pulse of an electric field in the time and frequency domain.

Time domain	Frequency domain
$f(x)sin(ax)$	$\frac{\hat{f}(\xi - \frac{a}{2\pi}) + \hat{f}(\xi - \frac{a}{2\pi})}{2i}$
$e^{-\alpha x^2}$	$\sqrt{\frac{\pi}{\alpha}} * e^{-\frac{(\pi\xi)^2}{\alpha}}$

Table 2.1: Time and frequency domain functions. (top) A function multiplied by a sine. (bottom) An exponential function.

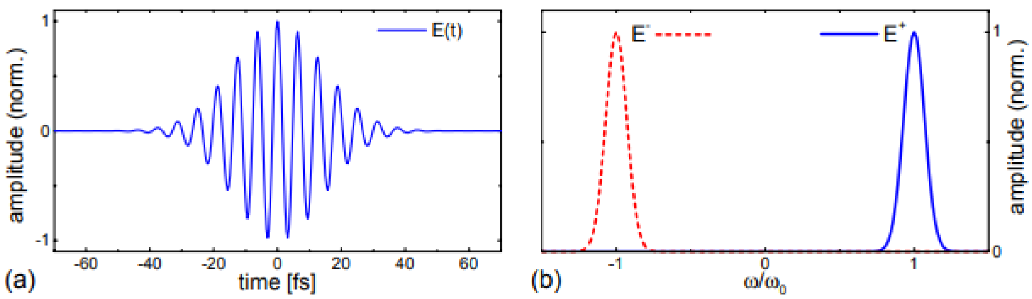

Figure 2.10: (a) Gaussian pulse in the time domain. (b) Fourier transform of the Gaussian pulse. (Merschdorf (2002) [32])

Besides changing the frequency of the Gaussian pulse, it is also possible to vary its expected value and variance. The expected value will not influence the Fourier transform but the variance will. By increasing the variance and therefore the pulse width, the peak widths in the frequency domain will decrease [34]. This can be seen in figure 2.11.

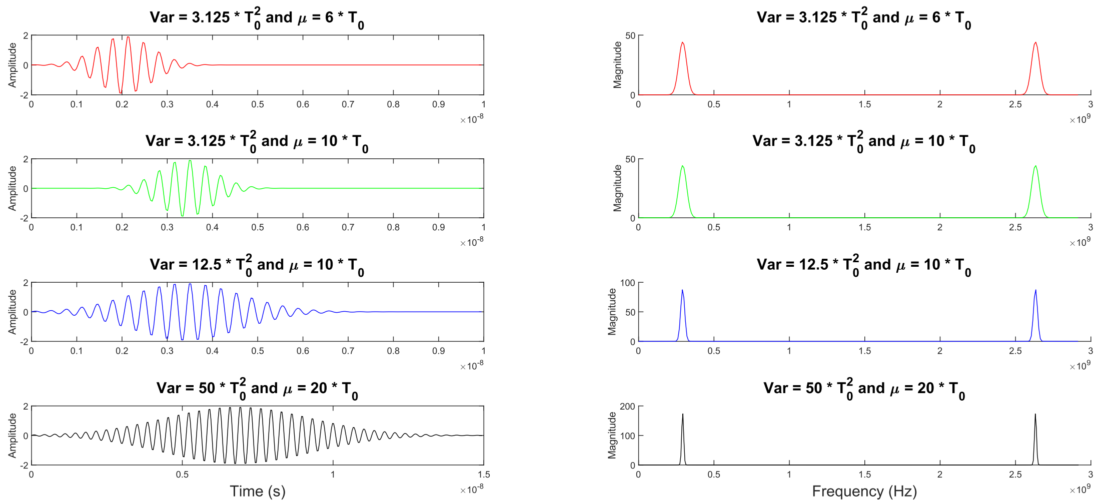

Figure 2.11: Influence of the expected value and variance on the Fourier transform of a Gaussian pulse in the time and frequency domain.

2.4.3. Excitation Location

By using a laser it is possible to excite the wave in different locations by altering the spot placement. The different excitation locations can influence the wave behaviour in varying manners. In this study, two locations are researched for acoustic wave guiding. The first location is inside the WG. This can be beneficial because here the wave will be confined by the surrounding phononic shield from the start of the wave propagation. Another possibility is to excite the wave at a distant location from the start of the WG. By having the acoustic wave travel some distance it will start to resemble a plane wave when it reaches the start of the WG. This plane wave will have a large component traveling along the desired propagation direction and less transverse propagation. In figure 2.12 a representation of how the spot excitation becomes a plane wave is shown.

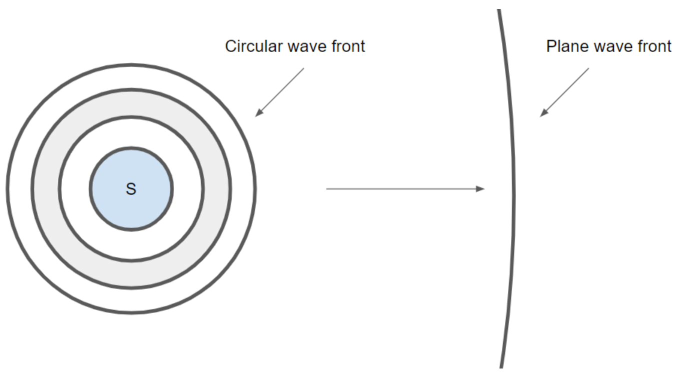

Figure 2.12: The spot excitation, blue shaded area, radius will increase over time for wave fronts traveling outwards. At some point, these circular wave fronts start to resemble plane wave fronts, as seen on the right.

2.4.4. Laser Detection

Pump-probe pulsed laser setups can be used to measure the deformation of suspended membranes. Here, the pump ($\lambda = 1560nm$) excites the acoustic wave and the probe ($\lambda = 780nm$) is used for detection. Both are pulsed lasers ($< 100fs$). By having the lasers synchronized to send pulses every $10ns$, it is possible to measure their response at different points in time by changing the delay between the pump and probe pulses. [24]

The probe detects the amount of reflected light coming from the sample, which is related to the amount of sample deformation. This works on the principle of a changing reflective index of the sample material caused by the strain that is inflicted on it.

What makes amplitude imaging difficult is that the wave amplitude scales inversely with frequency, meaning that high frequency vibrations have small deformations. Current measuring techniques have successfully measured GHz vibration amplitudes as low as one picometer, $1pm$ [40]. However, the available equipment used for this thesis has a limit of close to $15pm$.

2.5. Simulating Elastic Waves

For time explicit elastic wave simulations done in COMSOL, the mesh size and boundary conditions play a vital role in finding the correct solution.

When simulating in the frequency domain, the edge of the model is usually given a perfectly matched layer (PML) boundary condition. This boundary is used to absorb all incident energy. In the time domain, this PML is not available. Adding absorbing layers or domains will have the same characteristics as using a PML. By simulating a spring foundation including viscous damping, one can create such absorbing domains. The only goal of this domain is to absorb all the energy. Therefore, the damping constant needs to be sufficiently high.

Elastic wave simulations require the use of a specific mesh size. This size is influenced by the wavelength and typically 1 to 2 mesh elements are needed per wavelength. The shortest wavelength that is present in the simulation dictates the mesh size, as seen in equation (2.7). Where h_{max} is the maximum element size, c_{min} is the slowest wave speed and f_{max} is the maximum frequency used in the model. [14] [15]

$$h_{max} \leq \frac{c_{min}}{f_{max}} \frac{1}{1.5} \tag{2.7}$$

2.6. State of the Art: Suspended Membrane Waveguides

This section will describe the current state of the art regarding suspended membrane waveguides discussed above. Figure 2.13 displays the suspended WGs of the discussed papers. After the overview, a conclusion about the existing work is given.

Patel et al. (2017) present a single-mode phononic wire. Their goal is to design and demonstrate wires for phonons that transmit information with little loss or scattering across a chip. The WG is fabricated by introducing a line defect into a square lattice PnC possessing a full bandgap. This ensures that only a single propagation mode is passed within a large frequency range. The WG is made from a suspended film of Silicon with a thickness of $220nm$ and a length of approximately $2mm$. Their design is shown in figure 2.13 (1). [35]

Kurosu et al. (2018) demonstrate a temporal pulse manipulation in a dispersive one-dimensional PnC WG enabling ultrasonic wave propagation control. Due to the group velocity dispersion (GVD) effect, ultrasonic waves traveling through the WG experience pulse broadening. However, this GVD effect can also be used to compensate for the frequency modulation of the initial pulse that leads to temporal focusing. The PnC WG is a $1mm$ long and $22um$ wide membrane made from a GaAs/AlGaAs heterostructure with air holes periodically spaced with a pitch of $8\mu m$. Phonons are created via electrostatic Gaussian pulse excitation done at both ends of the WG resulting in ultrasonic vibrations. The experiments are done at room temperature. Their design is shown in figure 2.13 (2). [23]

Wang et al. (2019) demonstrate a hexagonal boron nitride (h-BN) PnC WG building block with band gaps in the radio frequency (RF) range. $15 - 24MHz$ wave propagation frequencies over a distance of $1.2mm$ are realized. The device is fabricated on $290nm$ SiO_2 on Si supporting substrates that carry $120nm$ thick h-BN layers. The WG is $12\mu m$ wide and has a maximal length of $165\mu m$ caused by fabrication difficulties. Because of the large elastic impedance mismatch, the acoustic energy loss is low and the wave is efficiently confined in the suspended WG. The phonons are photothermally excited by a $405nm$ blue laser and the detection is done by optical interferometry with a $633nm$ red laser. Their design is shown in figure 2.13 (3). [45]

Mauranyapin et al. (2021) present virtual phonon coupling between transverse mechanical elements, by tunneling through a zero-mode acoustic barrier. The WG is fabricated from $80nm$ high stress, $1GPa$, SiN membrane on a Si substrate. The SiN membrane is made up of a far-subwavelength square hole lattice. Acoustic waves are electrostatically excited in the low MHz range. Their design is shown in figure 2.13 (4). [30]

Madiot et al. (2022) show the generation of GHz phonons in a suspended 2D Si PnC. Their system includes an air-slot inside the WG to transform it into an optomechanical platform. This enables the excitation of in-plane localized phonons around $6.8GHz$. The air-slot is made by bringing two identical PnCs close together. The PnCs consist of shamrock holes in a hexagonal lattice structure. Their design is shown in figure 2.13 (5). [28]

From the literature, it is found that suspended structures offer a viable solution to acoustic wave data transfer for on-chip devices. Fabrication of nanoscale feature sizes in square and hexagonal crystal lattices enables the development of bandstructures possessing GHz bandgaps. Straight WGs constructed of line defects inside PnCs are experimentally shown to support in-plane vibrations at GHz frequencies. By using high stress SiN, the design of Mauranyapin et al. (2021) is able to observe out-of-plane low MHz vibrations at room temperature.

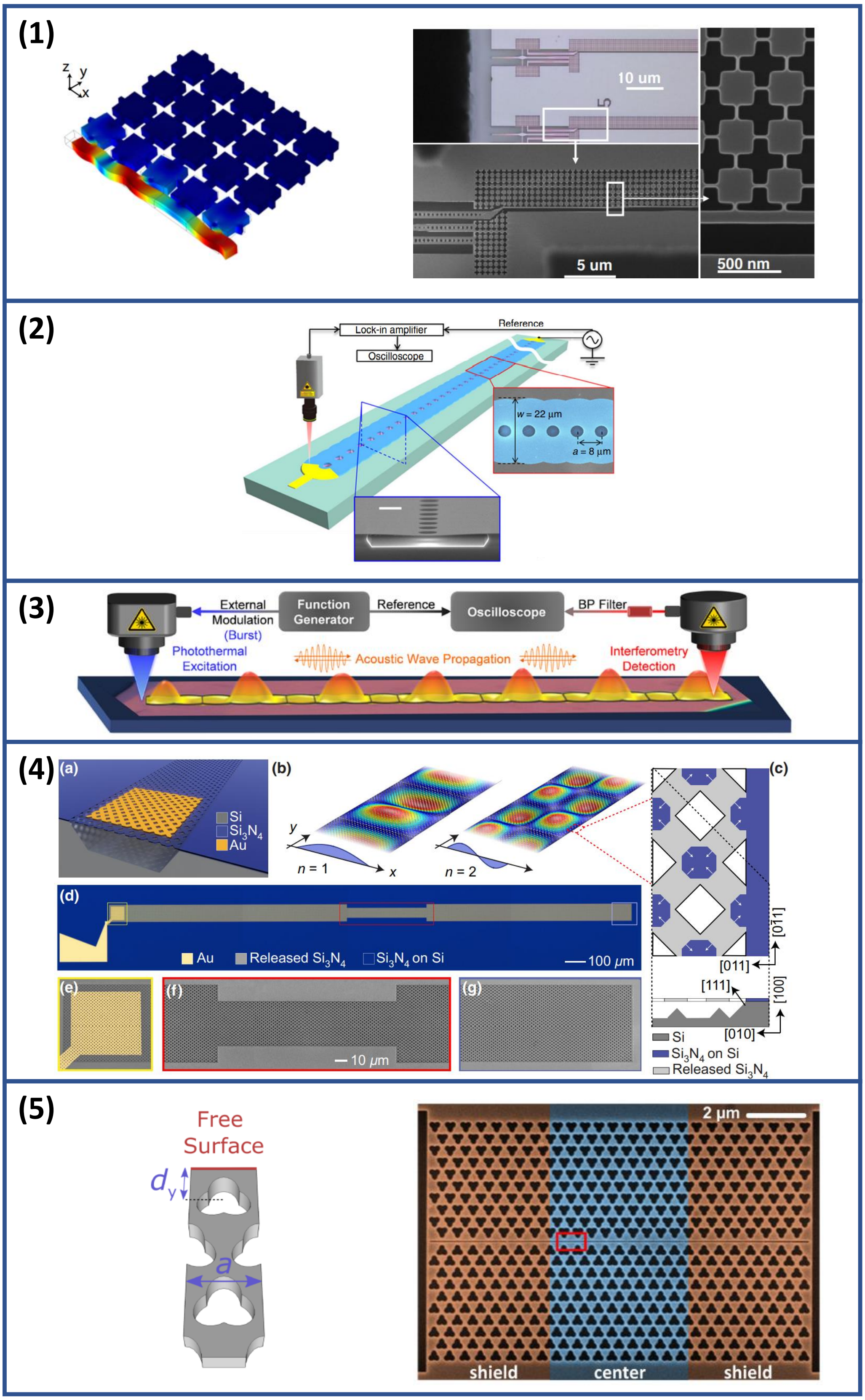

Figure 2.13: Suspended membrane waveguides of section section 2.6. (1) Patel et al. (2017) [35] (2) Kurosu et al. (2018) [23] (3) Wang et al. (2019) [45] (4) Mauranyapin et al. (2021) [30] (5) Madiot et al.(2022) [28]

2.7. State of the Art: Acoustic Wave Guiding and Beam Splitters

In this section, the current state of the art of acoustic wave guiding together with acoustic beam splitters is given. Figure 2.14 and figure 2.15 display the acoustic wave bending and beam splitter devices of the discussed papers. After the overview, a conclusion about the existing work is given.

Khelif et al. (2004) demonstrate one of the earliest experiments of guiding and bending acoustic waves. A PnC is made from a 2D square lattice of steel cylinders immersed in water. A full bandgap between $250 - 325kHz$ is obtained and a WG is formed by introducing a line defect by removing rods from the lattice. It is found that the wave propagation distance (the total traveled wave distance inside the PnC) is lower by widening the WG because of destructive interference occurring in the wider WG. Adding two $90°$ turns into the lattice results in a small drop of propagation. Their design is shown in figure 2.14 (1). [20]

Kaya et al. (2014) present a 2D interferometer with phononic mirrors and a beam splitter using kHz self-collimating waves. The PnC consists of a square lattice of steel cylinders in water. Beam splitters are obtained by adjusting the radii of the steel cylinders along a line defect domain. Mirrors are made by adjusting a line defect domain such that no wave propagation is possible in that direction, therefore reflecting the wave. Figure 2.15 (2) displays their acoustic interferometer. [19] A similar design is tested by Li et al. (2015). Adjusting the cylinder radii to split the incident wave is again shown here. Besides this, they also show a square rod PnC design. By introducing a line defect caused by changing the rod angle, it is also possible to fabricate a beam splitter. Figure 2.15 (3) displays their device. [27]

Tang et al. (2018) introduce a numerical concept of a one-way acoustic beam splitter. The goal is to split an incoming acoustic wave into multiple beams while reducing the backward transmission from the output ports. The PnC consists of water cylinders arranged in a hexagonal lattice immersed in mercury. Line defects of removed cylinders are used to confine the wave and a single hexagonal cavity defect is used to scatter the incident wave in multiple directions. Their numerical design is shown in figure 2.14 (2). [43]

Wang et al. (2019) present the first experimental demonstration of confined propagation and splitting of Lamb waves. Lamb waves are a form of guided waves present in thin plates or shell-type objects. The 2D PnC is made from a stainless steel slab with a square cross hole lattice. Mostly out-of-plane modes are electrostatically excited in the low kHz range. Line defects are used to guide the waves and the splitters consist of simple $90°$ junctions in the lattice. Splitting seems to happen evenly. However, the wave intensity experiences large drops after the splitter junctions. Their device is displayed in figure 2.14 (3). [46]

Zhang et al. (2020) present numerical demonstrations of SAW on a PnC made from cone-shaped micropillars attached to a half-space. By varying the pillar radius in the defect zone, the energy ratio of the beams can be adjusted. A one to three beam splitter and an MZI are designed. The device consists of a square lattice of cone-shaped pillars with a double pillar row line defect. The excitation is simulated as a plane wave source of $1.64GHz$. Their design is shown in figure 2.15 (1). [49]

Shelke et al. (2014) numerically demonstrate various devices using PnC consisting of a square lattice of polyvinylchloride cylindrical rods in air. One suggested design is that of a y-shaped ultrasonic beam splitter for in-plane kHz frequencies. Equal splitting of the energy is not possible since they excite under an incident angle. They propose that equal splitting could be possible with a design using a longer initial propagation before the splitter. Their y-shaped beam splitter is displayed in figure 2.14 (4). [41]

The literature shows that acoustic wave guiding and splitting in PnCs are done in two different ways. One way is to introduce multiple direction line defects that cause wave bending and splitting, seen in figure 2.14. Most designs use a liquid for the wave-supporting material. Only Wang et al. (2019) show out-of-plane wave splitting, using the solid material of the PnC itself as the wave-supporting material. The second method is to use self-collimating waves that are incident to line defects which alter the reflecting indexes, seen in figure 2.15. This is always done by using air as the wave-supporting material. No designs feature suspended structures or out-of-plane GHz frequencies. It is also noted that only the design of Tang et al. (2018) uses a hexagonal lattice for wave bending or splitting.

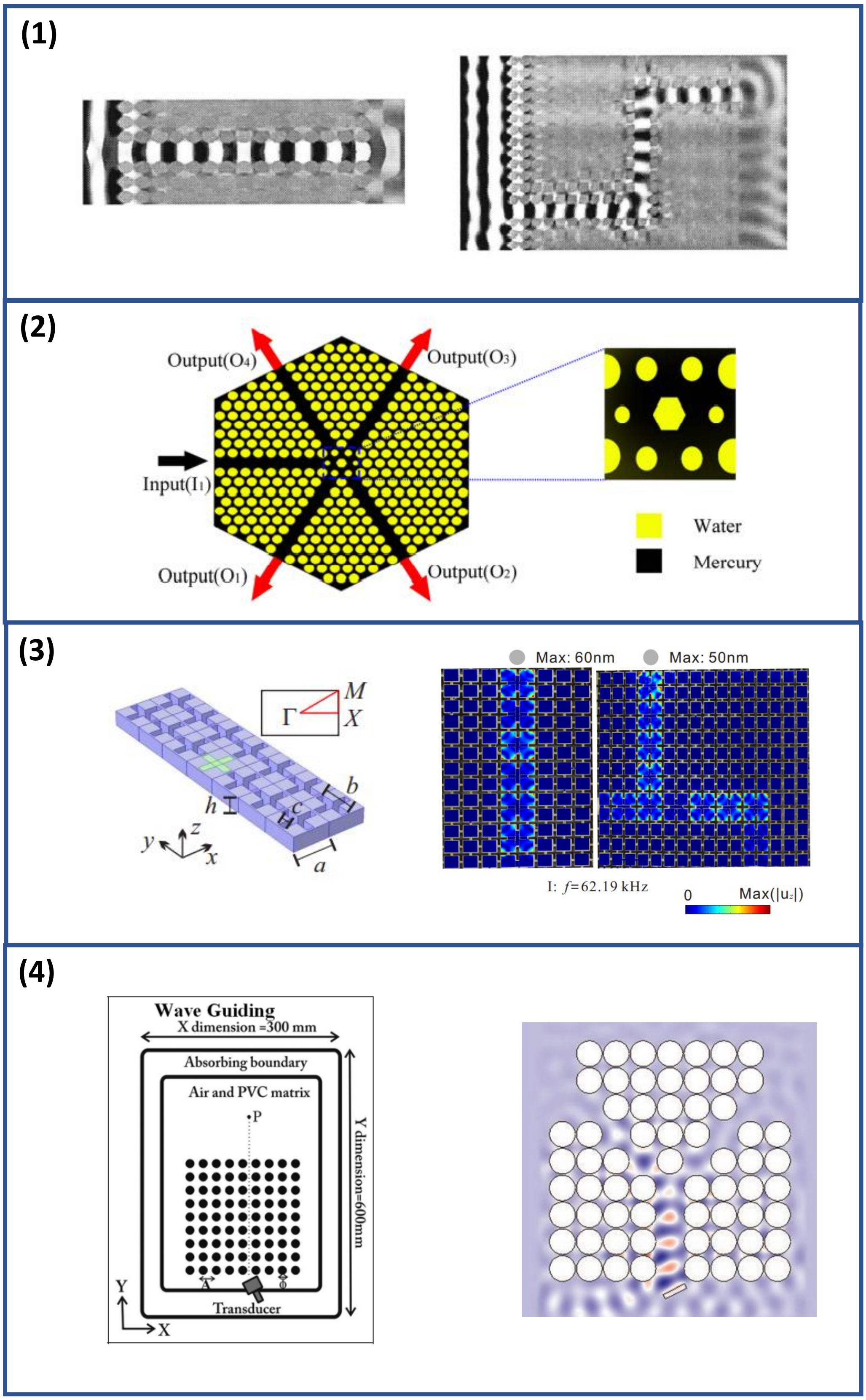

Figure 2.14: Multiple direction line defect splitters. (1) Khelif et al. (2004) [20] (2) Tang et al. (2018) [43] (3) Wang et al. (2019) [46] (4) Shelke et al.(2014) [41]

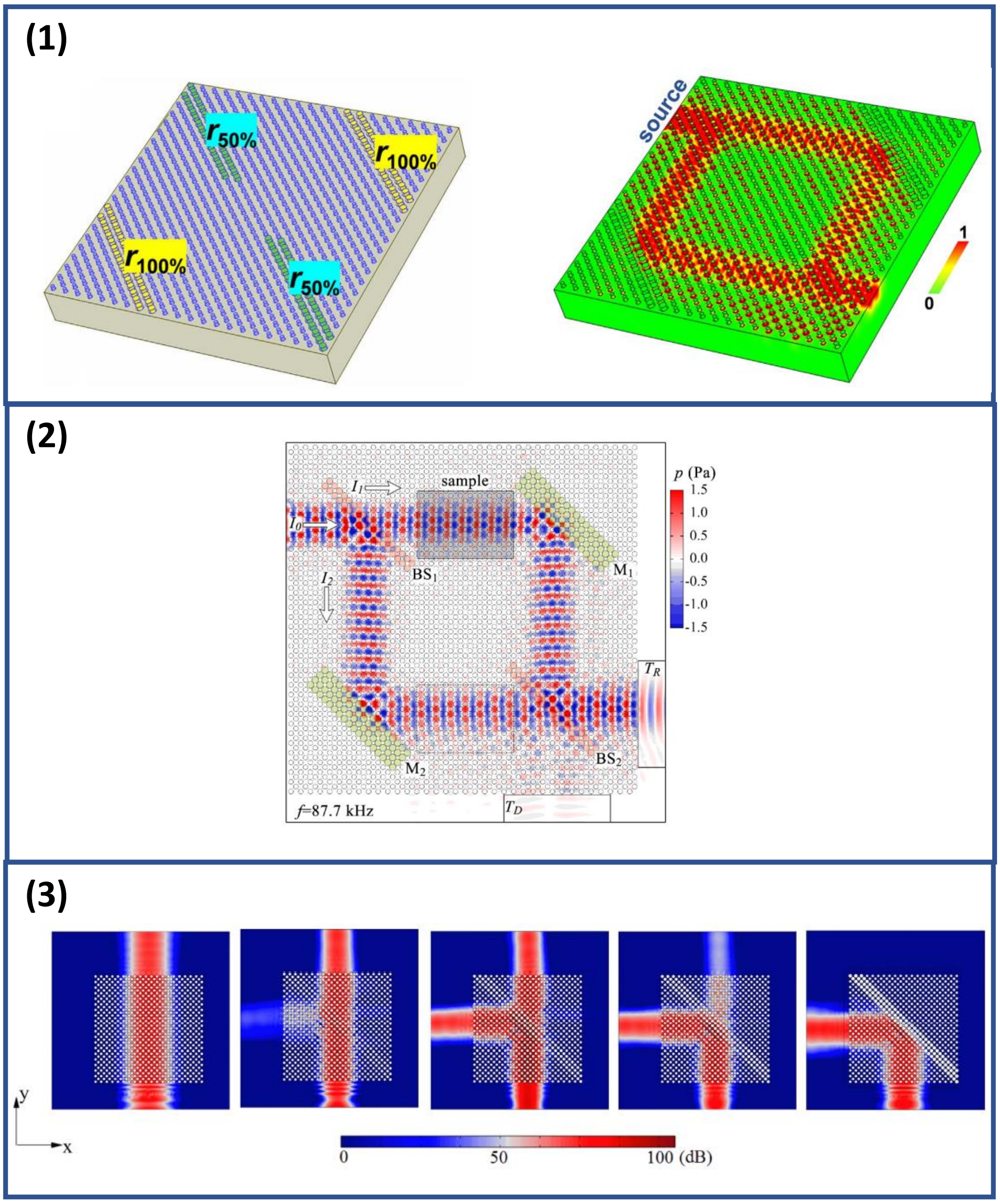

Figure 2.15: Self-collimating wave splitters. (1) Zhang et al. (2020) [49] (2) Kaya et al. (2014) [19] (3) Li et al. (2015) [27]

2.8. State of the Art: Phononic Integrated Circuits

This section involves a study proposing the implementation of phononic WGs into more complex phononic integrated circuits (PnICs). The study shows that these PnICs have a need for acoustic beam splitters.

Fu et al. (2019) present a PnIC made from a gallium-nitride-on-sapphire (GNOS) platform. Their system relies on acoustic velocity mismatch between the waveguide, substrate and surrounding environment. They claim this is more fabrication friendly than trying to create this complexity in suspended waveguides because of the 3D nature of the structures. Their PnIC design together with its cross-sectional energy density profile is displayed in figure 2.16.

The WG is optimised for frequencies around $100MHz$ ($50\mu m$ wavelengths) and is $5\mu m$ tall and $50\mu m$ wide. Actuation is done via an interdigital transducer (IDT), which converts RF photons to phonons. The IDT consists of two comb electrodes with parallel fingers and provides a periodically distributed electric field. Their results show that a high acoustic velocity mismatch is a possible solution for constructing PnIC parts, like straight waveguides and ring resonators. [9]

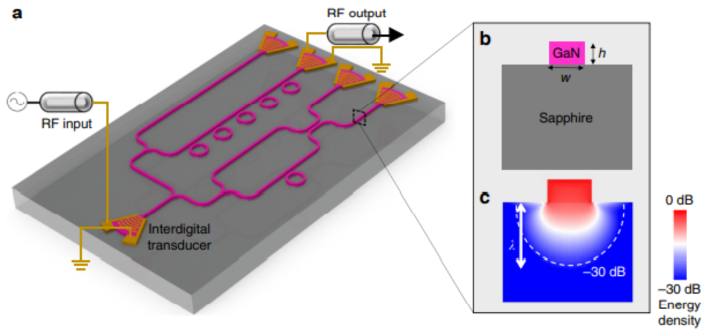

Figure 2.16: Phononic integrated circuit. (a) Schematic of a PnIC. Actuation is done by photon to phonon conversion by an IDT. The output converts the phonons back to photons using an IDT. (b) Schematic cross section of GNOS waveguide. (c) Simulated energy density distribution. Fu et al. (2019) [9]

2.9. State of the Art: Discussion

The PnIC concept discussed above shows an on-chip complex acoustic system consisting of multiple WGs and beam splitters. These large complex acoustic systems require low losses for sufficient wave propagation throughout the entire system. By utilizing an on-chip design, it is possible to operate under vacuum and cryogenic temperatures to lower the damping losses. This does mean that the wave supporting material cannot consist of a liquid or air type.

From the literature, it is found that suspended structures offer a viable solution to acoustic wave data transfer for on-chip devices. Straight WGs constructed of line defects inside PnCs are experimentally shown to support in and out-of-plane vibrations. The design of Mauranyapin et al. (2021) is able to observe out-of-plane MHz vibrations at room temperature with the use of high stress SiN.

Contrary to the straight suspended WGs, acoustic beam splitters have not been designed for on-chip use. The literature shows that acoustic wave guiding and splitting in PnCs are done in two different ways. One way is to introduce multiple direction line defects that cause the wave bending and splitting, seen in figure 2.14. Most designs use a liquid for the wave-supporting material. Only Wang et al. (2019) show out-of-plane wave splitting, using the solid material of the PnC itself as the wave-supporting material. However, this is not done at the microscale which is needed for on-chip designs. The second method is to use self-collimating waves that are incident to line defects which alter the reflecting indexes, seen in figure 2.15. This is always done by using air as the wave-supporting material.

Looking at the beam splitter designs found in the literature, it is noted that no designs are capable of on-chip beam splitting which is needed for integration into large complex PnICs. Therefore, a new type of beam splitter needs to be designed. In this study, the design principles of the suspended WGs found in the literature are used to design a beam splitter inside a suspended PnC for on-chip beam splitting.

3
Method

In this chapter, it is explained how the programs COMSOL 6.0 and Matlab 2020b are used to answer the research question that is set up in the previous sections. First, a quick overview of the COMSOL 6.0 file setup is given. Then, the initial design constraints and parameters are introduced. Next, the PnCs are designed and their bandstructures calculation is shown. Section 3.3 explains the first elastic wave simulations regarding the excitation methods. This is followed by the excitation frequency influence and splitter simulations. Finally, the complete splitter simulation is explained.

COMSOL 6.0 has a distinct file setup divided under multiple main tabs, each featuring its own subtabs. The main tabs consist of the ”Global definitions”, the ”Model”, ”Study” and the ”results” tab. In the ”Global definitions”, the used parameters are located. The ”Model” tab features the ’Geometry”, ”Material”, ”Physics” and ”Mesh” used in the simulation. The ”Study” tab describes the calculations by introducing calculation steps and configuring the used solver. The final tab is ”Results”, where the calculated outcomes from the ”Study” tab are found. Within ”Results” it is possible to make data sets, derived values, tables and plots.

3.1. Design constraints and Parameters

3.1.1. Material

The membrane is made from high stress ($1GPa$) Silicon Nitride, Si_3N_4. Minimum feature sizes are set at $100nm$. A membrane thickness of $80nm$ is used to stay within the limits of the minimum and maximum membrane thickness range.

3.1.2. Device requirements

From the found literature on PnCs, it is found that propagation distances often are between 10 and 40 lattice constants with some designs reaching 100 lattice constants. In order to find out if suspended structures are a solution for on-chip GHz beam splitters, the propagation distance needs to be comparable with other PnCs to validate the use of suspended structures. For the simulation, it is advantageous to make the simulated geometry small to reduce computation time. Therefore, a minimum wave propagation distance of 20 lattice constants is chosen as a requirement. This will keep the geometry size relatively small while still being comparable with the found PnCs in literature.

A lattice constant of $1\mu m$ is chosen as a starting point for the lattice design. The maximum simulation size is set at $40\mu m * 40\mu m$ to constrain the computation time.

To reduce the chances of the suspended membrane collapsing after fabrication. It is favorable to have a design where the PnC shield is on both sides of the WG. This will increase the support of the suspended structure.

As previously mentioned, there is a minimum measurable amplitude. In this study, the minimum measurable amplitude is set at $15pm$. The wave propagation distance is therefore measured to the point where the wave amplitude is above $15pm$.

3.2. Bandgap Simulations

Both a square and hexagonal crystal lattice bandstructure will be calculated. The difference between constructing a square or hexagonal lattice bandstructure is the unit cell geometry and the wave vector (k-vector). The other simulation steps are identical.

The bandstructure calculation involves a frequency response evaluation of the unit cell. The wave vector describes the travel direction of the wave. The wave number is the magnitude of the wave vector. By evaluating the frequency response over a range of wave vectors along the IBZ, the smallest symmetric area of the unit cell, a complete bandstructure is formed. By adding Floquet boundary conditions, the displacements of the unit cell edges are constrained. This is needed to simulate the periodic occurrence of the unit cell in the PnC. The wave vector evaluation along the IBZ edge is done by using a parametric sweep (from 0 to 3) of the wave number parameter k. The horizontal IBZ edge is defined from 0 to 1, the vertical IBZ edge from 1 to 2 and the diagonal IBZ edge from 2 to 3. For all k values, the lowest Eigenfrequency is found and plotted in the bandstructure.

3.2.1. Global Definitions

In the ”Global definitions”, a list of parameters that can be seen in appendix B are added. Where the lattice constant is taken from the previous sections. The hole radius, R, is chosen by maximizing the BG% discussed in section 2.3. The result is that the minimum feature size is the limiting factor for the hole radius.

3.2.2. Model

For the Geometry, the unit cell of the crystal lattice is drawn. In figure 3.1, the geometries of the square and hexagonal lattice are shown.

Following the geometry, a material needs to be assigned to the different domains that are present in the geometry. For the membrane, Silicon Nitride(Si_3N_4) is chosen from the built-in COMSOL material library. The holes are simulated as a vacuum. Therefore, their domains are deleted and the resulting boundaries will be sat as ”free boundaries” in the physics tab.

In the physics tab, solid mechanics is selected to perform general structural analysis. A 2D approximation using generalized plain strain is used to enable out-of-plane bending. The model is set to be a linear elastic isotropic material. The initial stress matrix is set up to have $1 * 10^9[N/m^2]$ along its diagonal.

For the boundary conditions, the vacuum border is set as a free boundary as mentioned before. Two periodic conditions are added to simulate the periodic array of unit cells in the complete PnC. The periodicity type is set as ”Floquet periodicity”. The Floquet conditions require an X and Y component of the k-vector for the periodic sweep along the IBZ edges. These can be seen in equation (3.1) and equation (3.2) for the square and hexagonal lattice respectively. The periodic boundaries for the square and hexagonal lattice can be seen in figure 3.2.

$$k_x \in [0; \frac{\pi}{a}] \quad \text{and} \quad k_y \in [0; \frac{\pi}{a}] \tag{3.1}$$

$$k_x \in [0; \frac{2\pi}{3a}] \quad \text{and} \quad k_y \in [0; \frac{2\pi}{\sqrt{3}a}] \tag{3.2}$$

The Mesh is set to be physics-controlled and the element size is ”normal”. The resulting meshes can be seen in figure 3.3.

3.2.3. Study

To calculate a complete bandstructure, the Eigenfrequency analysis needs to be swept across the edge of the IBZ. Therefore, a ”parametric sweep” is added for the k-vector. With starting value, 0, end value, 3, and 35 computational steps.

The Eigenfrequency solver is set to find the first 10 Eigenfrequencies in the GHz range.

3.2.4. Results

To plot the bandstructure, a 1D plot group is added to the results. A ”global” subnote is added to insert the y and x-axis data. The y-axis displays the frequency using the ”solid.freq” expression. The x-axis data consists of the ”outer solutions” of the k-vector.

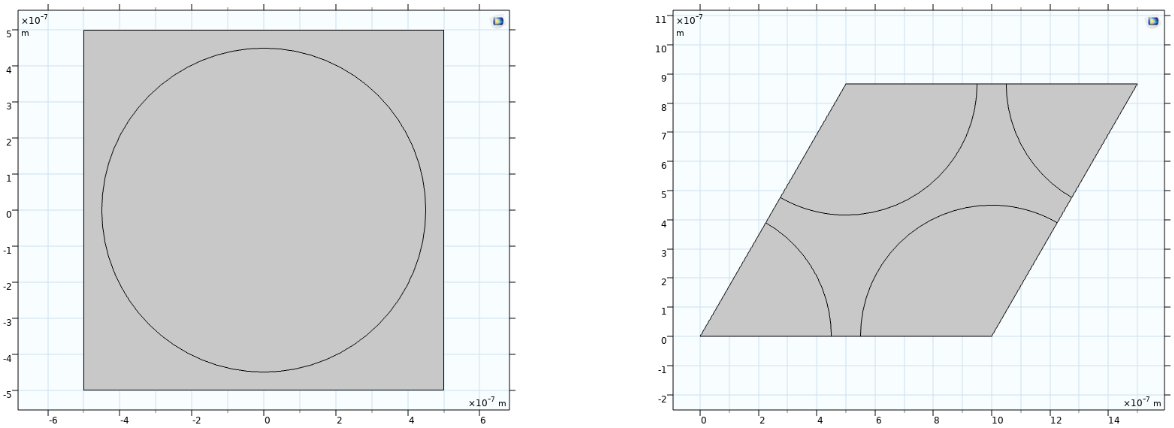

(a) (b)

Figure 3.1: (a) Square lattice unit cell geometry. (b) Hexagonal lattice unit cell geometry.

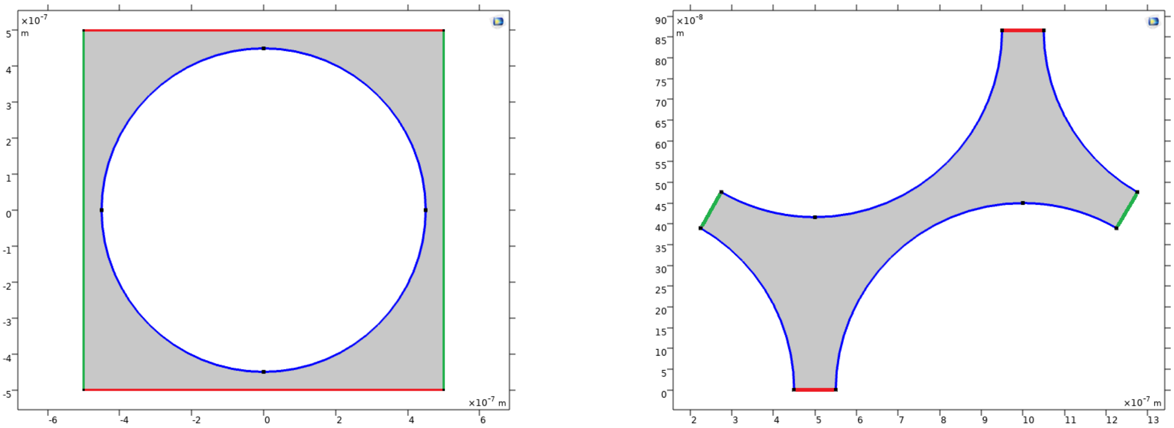

(a) (b)

Figure 3.2: Boundary conditions for the square lattice (a) and the hexagonal lattice (b). The blue boundary represents a free boundary. The red boundary represents periodic condition 1. The green boundary represents periodic condition 2.

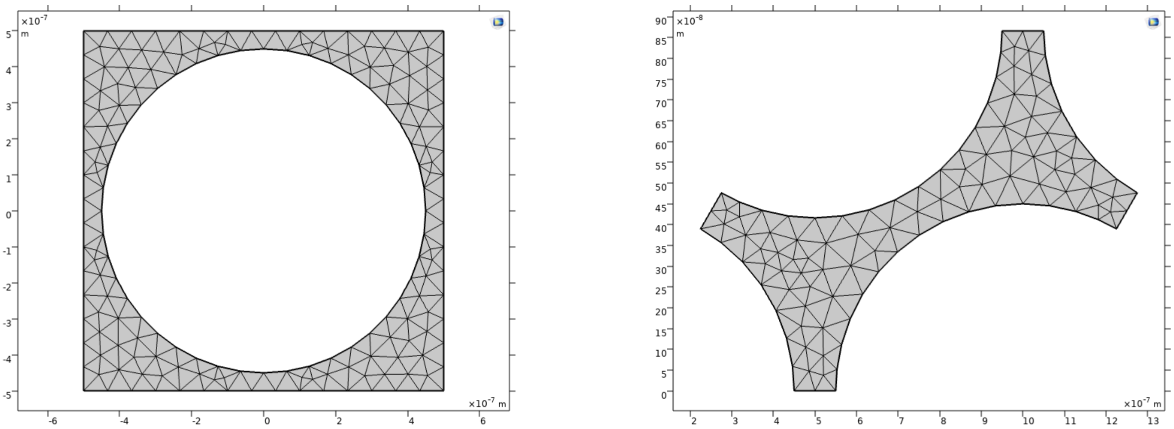

(a) (b)

Figure 3.3: (a) Meshed square unit cell. (b) Meshed hexagonal unit cell.

3.3. Straight Waveguide Excitation Method Simulations

This section describes the set up of the COMSOL simulations involving the influence of the excitation method on a straight waveguide. The hexagonal lattice resulted in the highest BG%, seen in section 4.1. Therefore, it is chosen to use the hexagonal lattice for the excitation method simulations. The excitation method is also not influenced by the used lattice, meaning that the results are transferable to the square lattice and only one lattice needs to be simulated.

3.3.1. Global Definitions

See appendix C for the used global definitions and parameters.

3.3.2. Definitions

In the definitions tab, an analytical function is added that will be used later on in the physics tab. In equation (3.3) this function is shown and figure 3.4 shows the plotted function. The mid-gap frequency from the highest BG% of the hexagonal lattice, $f_0 = 2.925GHz$, is used for input. For the amplitude, it is chosen to use a value of $2m/s$. Since this will result in a maximum out-of-plane wave excitation displacement of $100pm$, which is comparable with the measuring limit of $15pm$.

$$v_z = Amp * exp(-(\frac{t - 6T_0}{2.5T_0})^2) * sin(2\pi f_0 t) \tag{3.3}$$

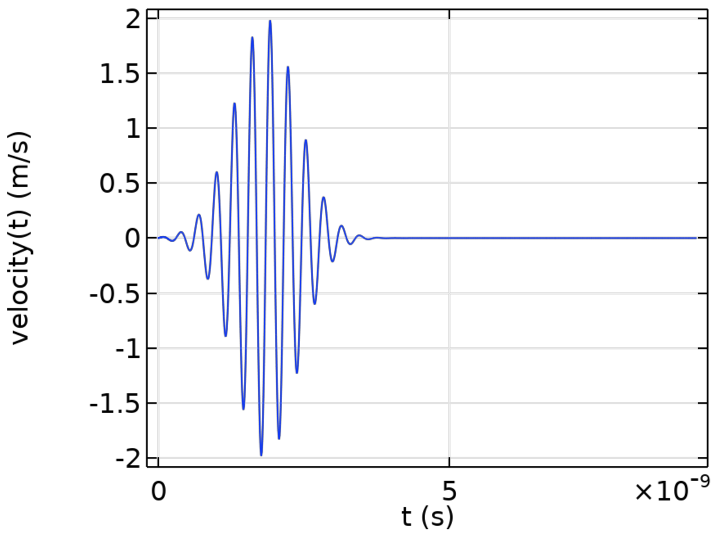

Figure 3.4: Plot of the analytical function for the prescribed velocity.

3.3.3. Model

A hexagonal array of circular holes is drawn for the PnC. A line defect is added to construct a WG with a width of half the lattice constant. The WG length is set to be 25 lattice constants. To reduce the computation time, only half of the device is simulated. This is done by introducing a symmetry axis along the y-axis further explained in the "study".

Two geometries are made to research the influence of the excitation location. One design will include a spot excitation inside the WG on different locations along the y-axis. The other design will feature a coupling wedge. This coupling wedge will simulate an excitation spot far away from the WG, thus a plane wave excitation can be assumed. The wedge width will be swept to find the highest confining wave design.

Regarding the spot excitation, the PnC is extended downwards from the $y = 0$ line for a length of $3a$. A circular spot shape is added inside the WG at the locations $(0, 0)$ and $(0, 0.5a)$. Finally, a simulation with a plane wave excitation at $(0, 0)$ is performed.

For both designs, the geometry above the $y = 0$ line is identical. $y = 0$ is also set to be the starting point of the wave propagation distance.

In figure 3.5 the final geometry of the straight WG and one iteration of both the spot and wedge excitations are shown. In appendix G the other designs are shown.

The material values are taken from the bandgap simulations section 3.2.2.

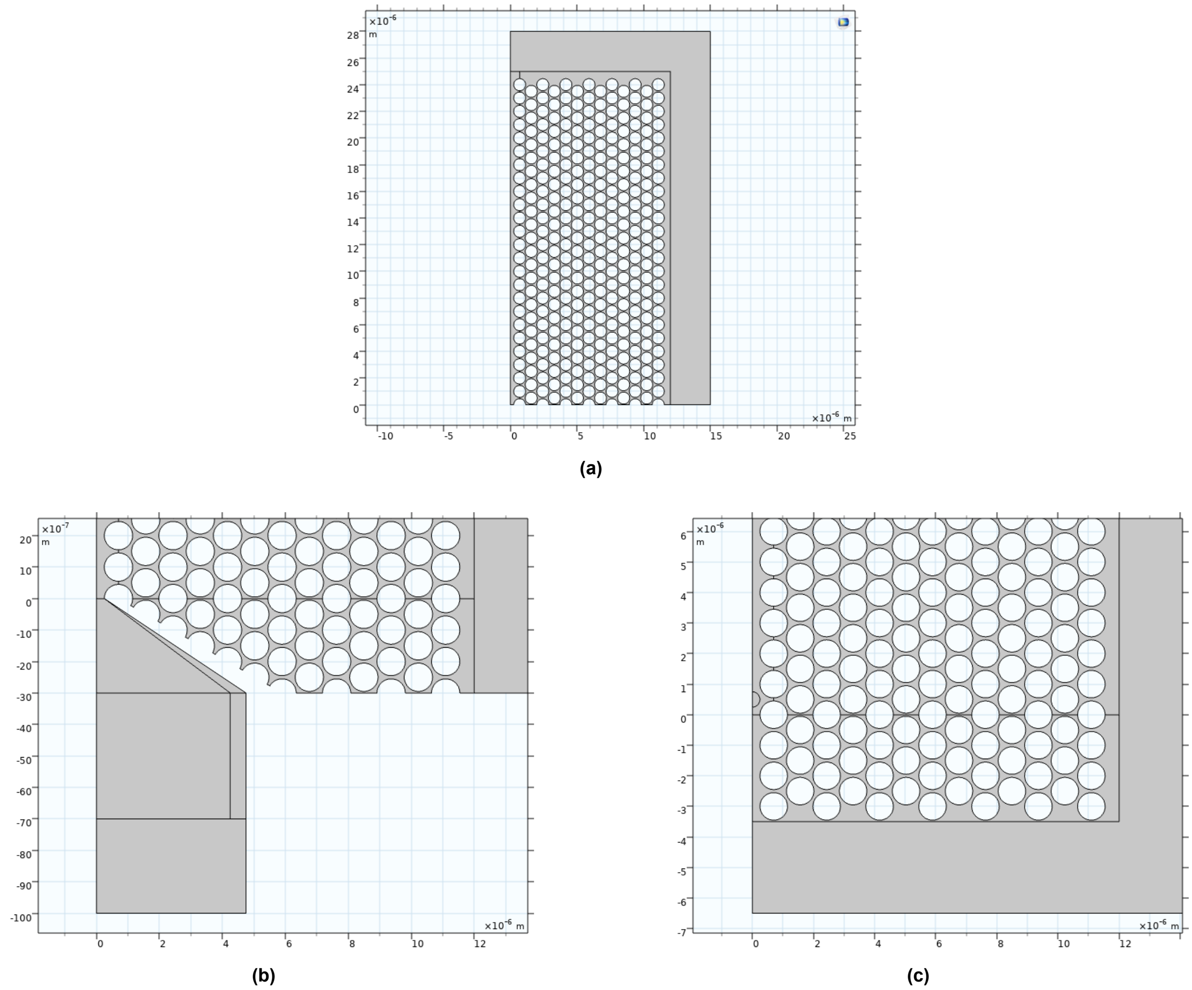

Figure 3.5: (a) Final geometry of the straight WG (b) 4x3 Wedge excitation (c) Spot excitation at (0, 0.5a)

Two different modules are used in the physics tab. Module one, "Solid Mechanics", is used to add the initial stress. Here, similar to the bandgap simulations, a 2D approximation is done using generalized plain strain to enable out-of-plane bending. Thickness is set to $80nm$ and the initial stress is added under the linear elastic material node. A thermal expansion domain is added to simulate at room temperature, $293.15[K]$.

For the boundary conditions, fixed constraints are added to attach the device to the world and a symmetry boundary condition along the y-axis is used to simulate the other half of the device.

In the second module, "Plate", the out-of-plane wave is added to the simulation. The domain settings are taken from the first step except for the two added domains, "thickness and offset" and "Spring foundation". The thickness of the model needs to be defined in the separate thickness domain. Here, again $80nm$ is selected. An absorbing domain is added in the form of a spring foundation and needs to include a sufficiently high viscous damping value. For these simulations, a damping constant per unit area of $d_A = 1 * 10^7[N * s/(m * m^2)]$ provides enough damping to achieve full absorption.

For the boundary conditions in the "plate" module, a prescribed velocity is added to the other boundary conditions present from the first module. The analytic velocity function from the definitions is added to the prescribed velocity in the z-direction. The study will be time dependent, thus the velocity function is also set to be time dependent, $velocity(t)$. figure 3.6 and figure 3.7 show the boundary and domain conditions for both excitation methods.

Two different mesh sizes are chosen. For the WG and PnC shield domain, a maximum mesh size of $\lambda/1.5$ is chosen. The wedge and spring foundation domains are meshed using a fine mesh size. figure 3.8 shows the used meshes.

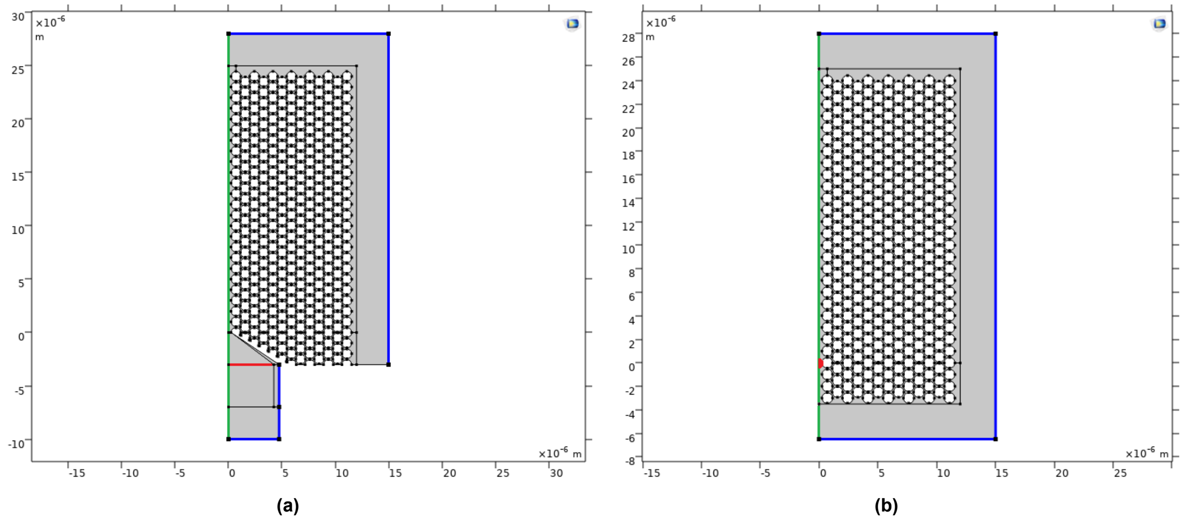

Figure 3.6: Boundary conditions for the wedge (a) and spot (b) excitation. Blue boundaries indicate the fixed constraints. Green boundaries indicate the symmetry along the y-axis. The red spot boundary indicates the prescribed velocity.

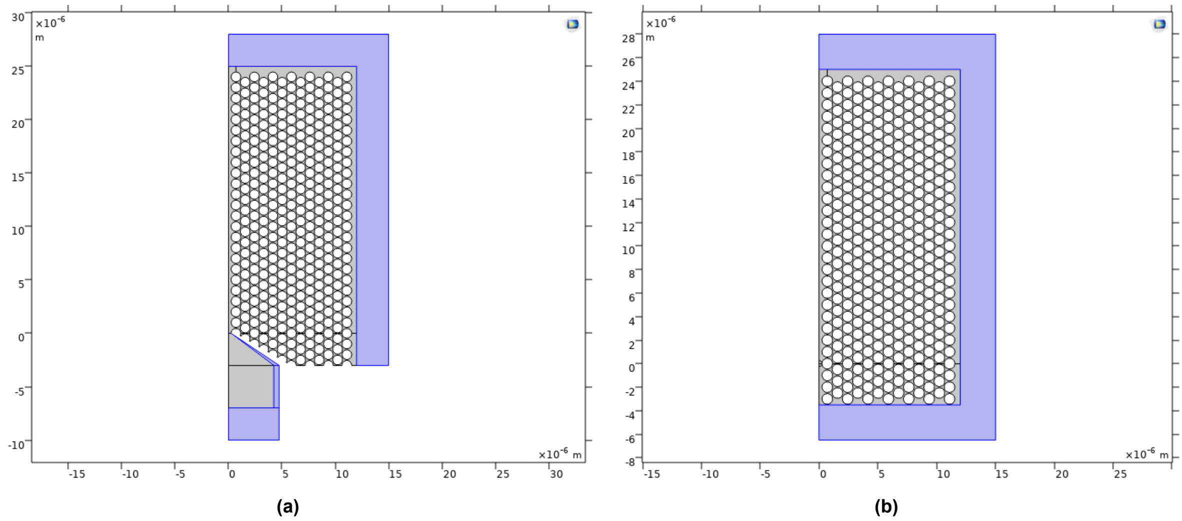

Figure 3.7: Spring foundation domains for the wedge (a) and spot (b) excitation.

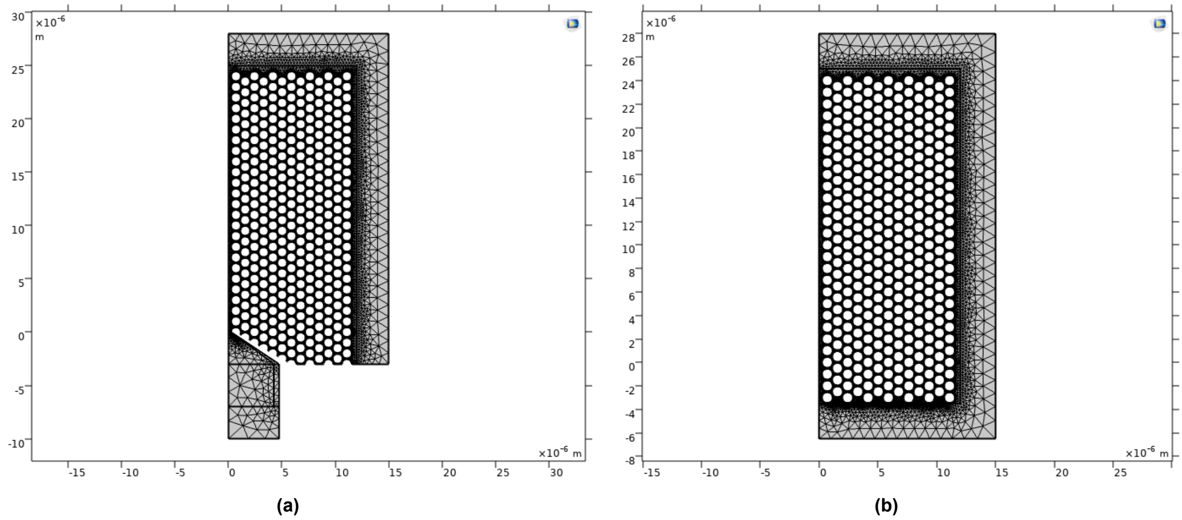

Figure 3.8: Meshed geometries for the wedge (a) and spot (b) excitations.

3.3.4. Study

In the study, a single time dependent calculation step is added to solve the wave propagation. The output times are done in a range from 0 to $time$ with a time step, dt. For a complete simulation, the total energy has to return to zero at the final step. It is found that $time = 5 * 10^{-8}s$ is sufficiently long for this. The solver solves for both the ”Solid Mechanics” and the ”Plate” physics modules.

3.3.5. Results

Results for the out-of-plane motion are plotted in a 2D surface plot group. See section 4.2 for the found results. The Z-component of the surface displacement is plotted from above in 2D with the ”plate.w” expression in combination with a linear symmetric scale.

A total energy calculation is done for the WG and the Shield domain separately. This involves a surface integration across the domains seen in figure 3.9 and figure 3.10. The total energy consists of the sum of the ”Stored energy density” (plate.Wh) and the ”Kinetic energy density” (plate.Wk). The resulting tables are then exported to Matlab for further analysis.

Appendix D shows one of the total energy calculation codes. Here, the total energies for the WG and Shield domains are calculated by first adding the stored and kinetic energy columns together and then multiplying these values by the membrane thickness.

The total WG and Shield energies over time are then plotted separately in the same figure. The ”trapz” function is used to calculate the area under these energy curves. The confinement performance metric is then calculated by dividing the total WG energy by the total WG+Shield energy.

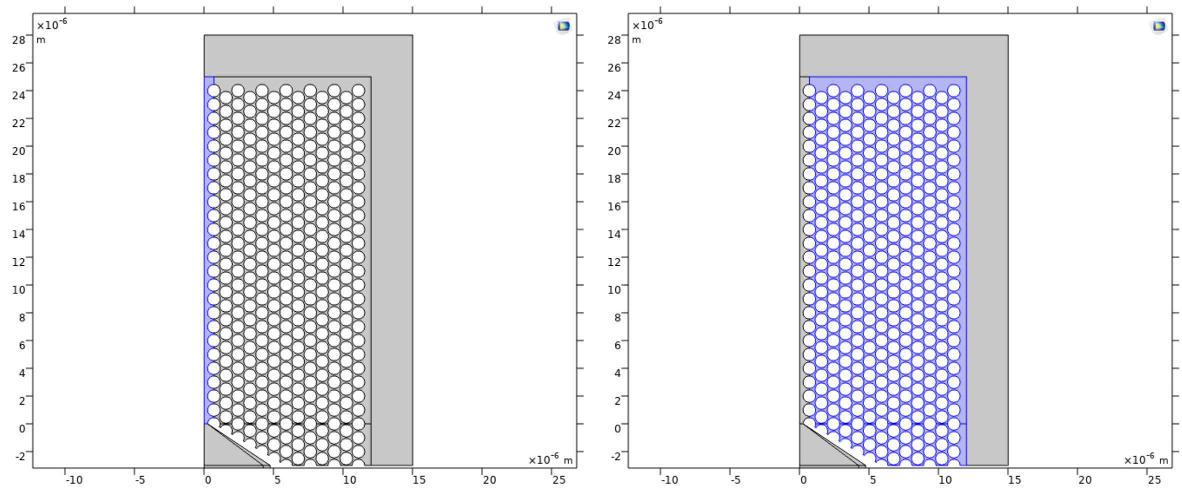

(a) (b)

Figure 3.9: Selection for the total energy calculation in the Wedge simulations. (a) WG domain (b) Shield domain.

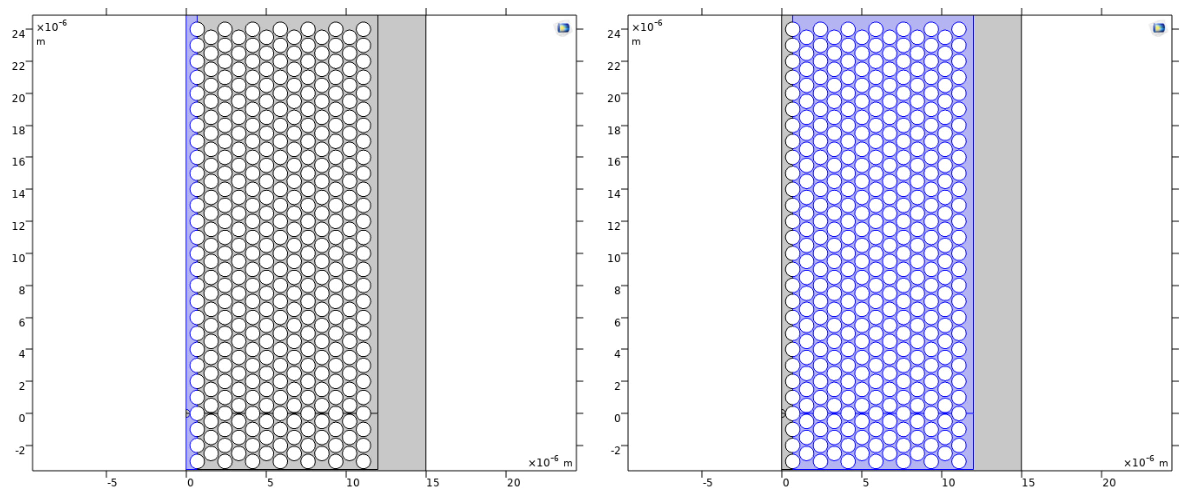

(a) (b)

Figure 3.10: Selection for the total energy calculation in the Spot simulations. (a) WG domain (b) Shield domain.

3.4. Excitation frequency influence simulations

For these simulations, the COMSOL model settings of the 4x3 wedge straight WG simulation are used. Only the input frequencies are varied to study their influence on the wave confinement.

3.4.1. Matlab: FFT

For the Gaussian sine, equation (3.3) is used.

Appendix E shows the MATLAB code used to calculate the FFT of the Gaussian sine input signals with different input frequencies. By having different input frequencies, the Fourier transform shifts in the frequency domain. Altering the input frequency has less influence on the low frequency peak location than on the high frequency peak. This means that the lower frequency peak always is outside of the bandgap. Therefore, mainly the higher frequency peak is looked at for its location w.r.t. the bandgap.

Five frequencies are analysed in their confinement performance. It is chosen to focus on the bandgaps with the highest BG%.

1. 2.925GHz: Mid-gap frequency
2. 2.450GHz: High frequency peak at the bottom of the bandgap
3. 3.250GHz: High frequency peak at the center of the bandgap
4. 3.975GHz: High frequency peak at the top of the bandgap
5. 1.000GHz: Control frequency were both peaks lay outside of the bandgap

Figure 3.13 shows the results for finding the optimal frequency regarding the square lattice design. This will be used when designing the square lattice splitter in the next section.

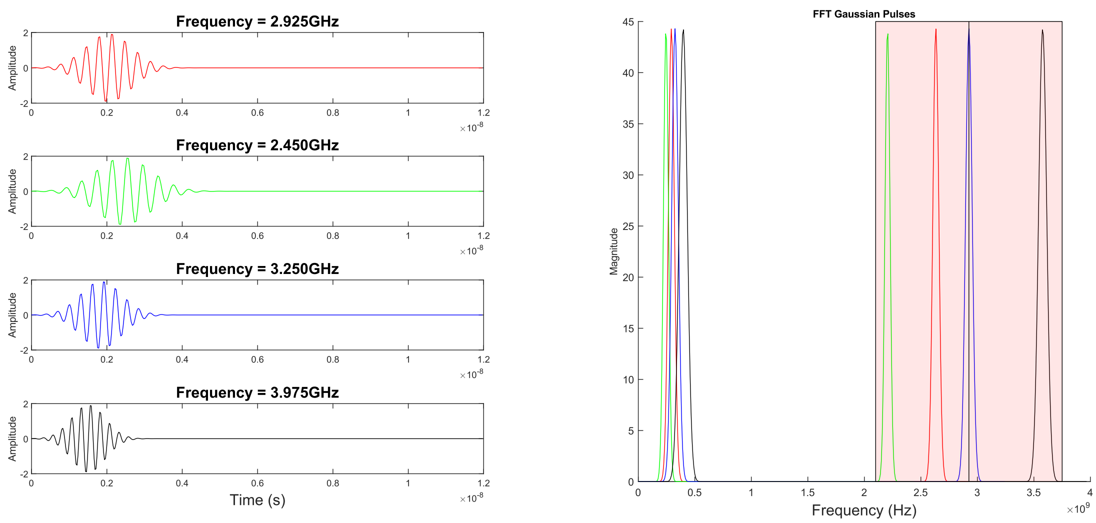

Figure 3.11: (a) Gaussian pulses with frequencies $1-4$. (b) Gaussian peaks in the frequency domain. Colors represent the different frequencies seen in "(a)". red shaded area indicates the Hexagonal lattice 1st bandgap region with the black vertical line being its center.

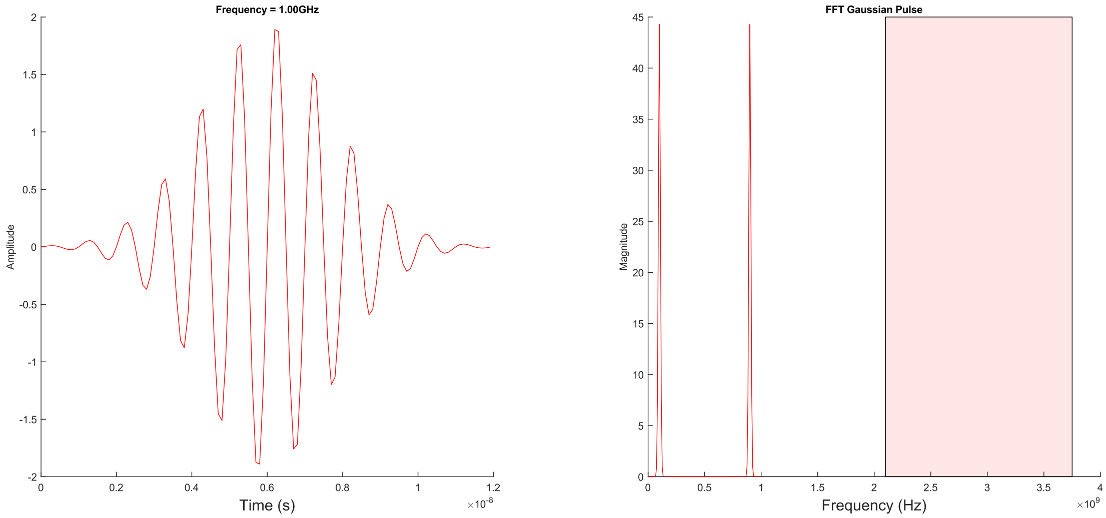

Figure 3.12: (a) Gaussian pulse with $f = 1.00GHz$ (b) Gaussian peaks in the frequency domain. Red shaded area indicates the hexagonal lattice 1st bandgap region.

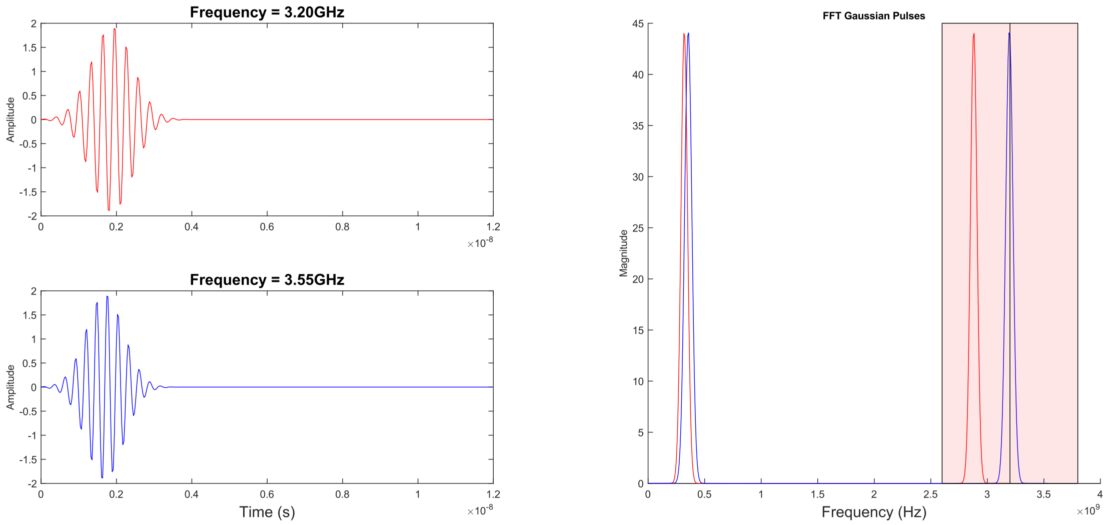

Figure 3.13: (a) Gaussian pulses with the different frequencies. (b) Gaussian peaks in the frequency domain. Colors represent the different frequencies seen in "(a)". red shaded area indicates the square lattice 1st bandgap region with the black vertical line being its center.

3.5. Splitter Simulations

See appendix F for the used global definitions and parameters. The study steps for the splitter simulations are taken from section 3.3.4.

3.5.1. Definitions

The analytic function from equation (3.3) is used in combination with the highest confining frequency, found in section 3.4. This results in $f_0 = 3.25GHz$ for the hexagonal lattice splitter and $f_0 = 3.55GHz$ for the square lattice splitter.

3.5.2. Model

In the splitter simulations, several WG widths are investigated for their influence on the wave confinement. The WG width is defined as the distance between opposite holes across the WG. In both Hexagonal and Square lattice designs, the WG widths of $0.5a$, $0.75a$, $1.00a$ and $1.25a$ are simulated. The geometries of the Hexagonal and Square lattice splitters with a WG width of $1.00a$ are shown in figure 3.14. The other WG width designs are present in appendix H.

The WG before and after the splitter are referred to as WG1 and WG2 respectively. In the hexagonal lattice splitter design, WG1 has a length of $10a$ and WG2 has a length of $13a$. This results in a total WG length of $23a$. The Square lattice splitter design has a total WG length of $20a$. Where both WG1 and WG2 have a length of $10a$.

The remaining model settings regarding the domains, boundary conditions, physics modules and mesh are taken from the previously discussed simulations. The boundary conditions, spring domains and meshes can be seen in figure 3.15, figure 3.16 and figure 3.17 respectively.

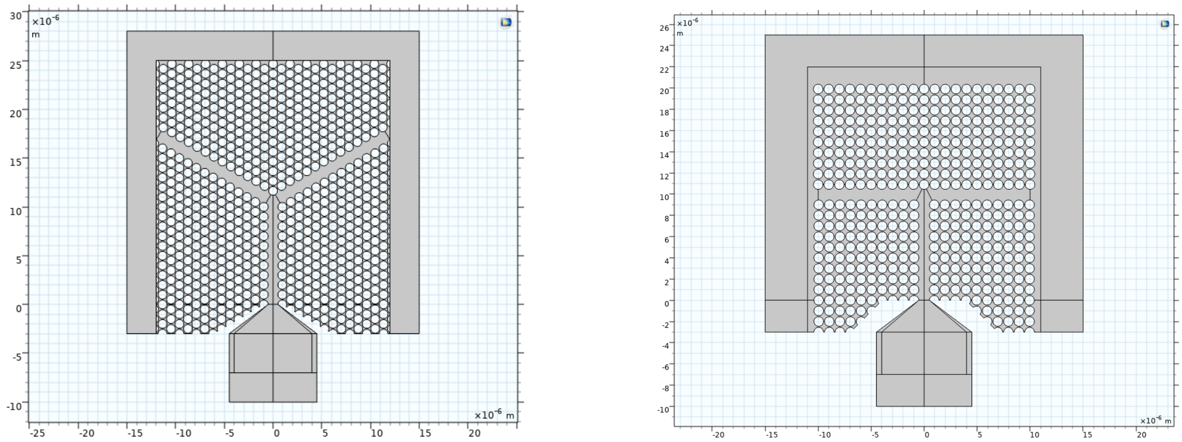

(a) (b)

Figure 3.14: (a) Hexagonal lattice splitter design. (b) Square lattice splitter design.

3.5.3. Results

See section 3.3.5 for the results settings. The domains used for the total energy calculations in the WG and Shield are shown in figure 3.18 and figure 3.19.

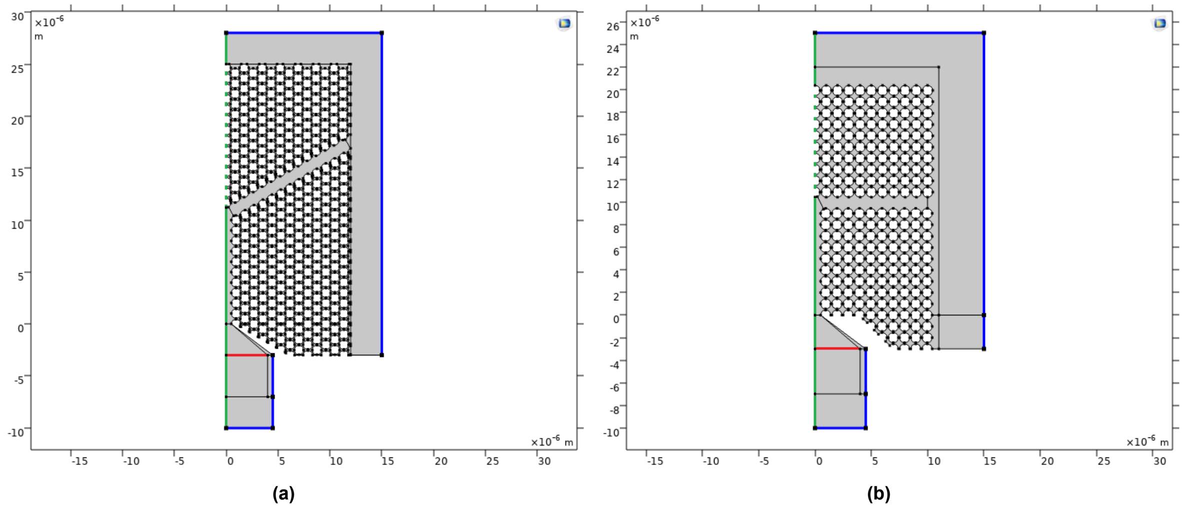

Figure 3.15: Boundary conditions for the hexagonal (a) and square (b) splitters. Blue boundaries indicate the fixed constraints. Green boundaries indicate the symmetry along the y-axis. The red boundary indicates the prescribed velocity.

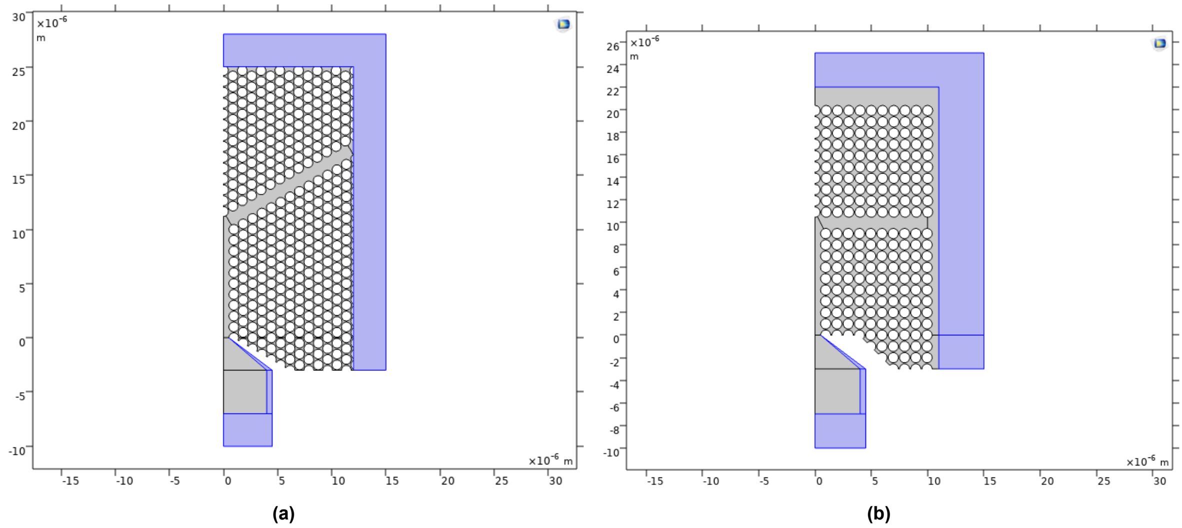

Figure 3.16: Spring foundation domains for the hexagonal (a) and square (b) splitters.

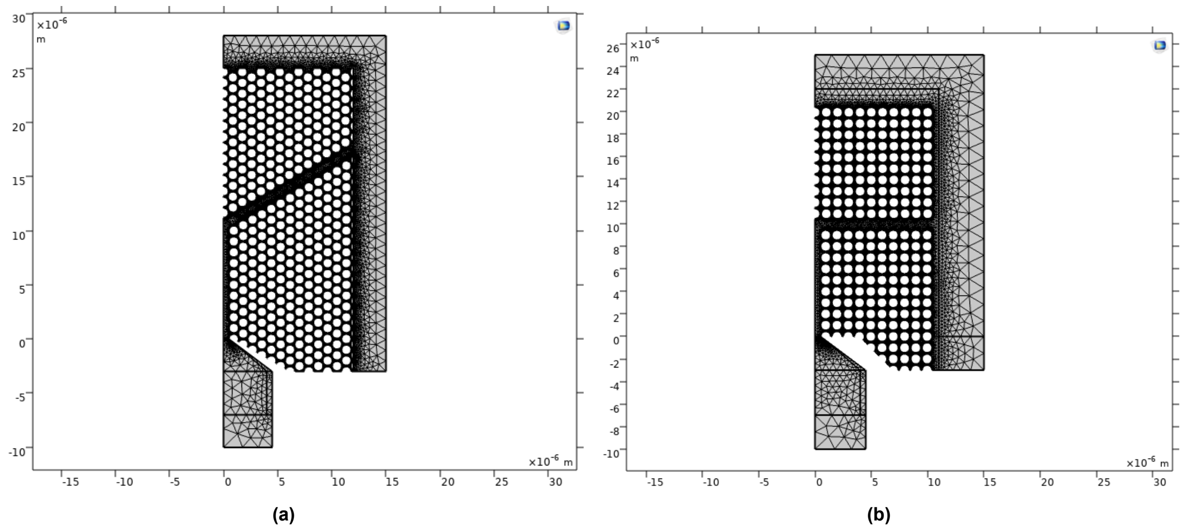

Figure 3.17: Meshed geometries for the hexagonal (a) and square (b) splitters.

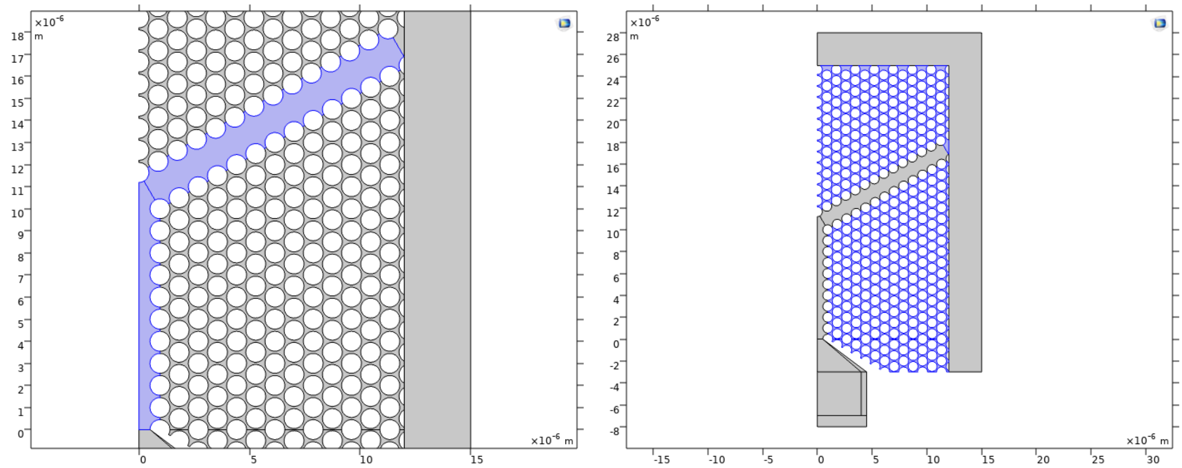

(a) (b)

Figure 3.18: Selection for the total energy calculation in the Hexagonal lattice splitter simulations. (a) WG domain (b) Shield domain.

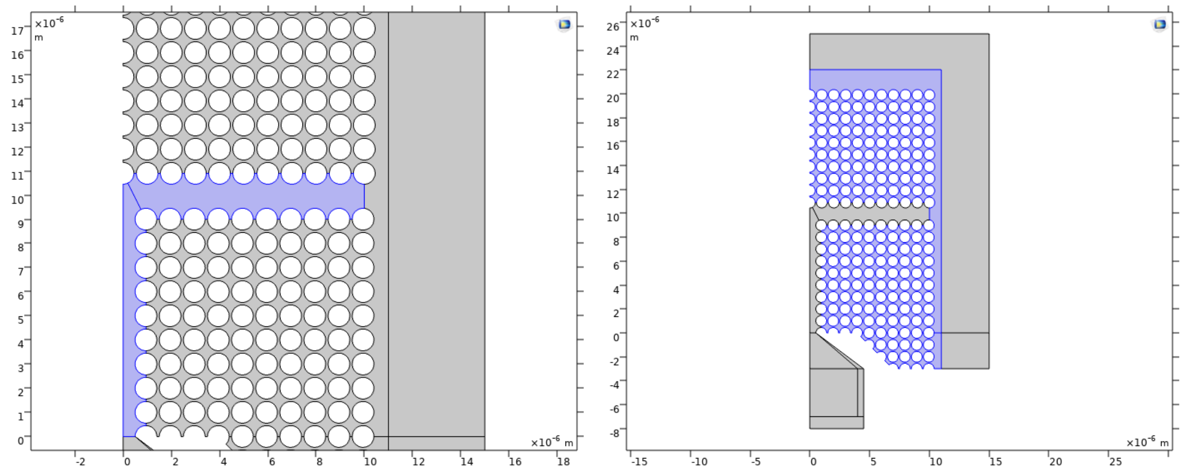

(a) (b)

Figure 3.19: Selection for the total energy calculation in the Square lattice splitter simulations. (a) WG domain (b) Shield domain.

3.6. Complete Splitter Simulation

3.6.1. Splitter Efficiency

To define the splitter efficiency, a simulation without the symmetry boundary condition is needed. This is done by using the simulation setup from the hexagonal lattice splitter with a WG width of $1.00a$. The difference is that now the complete geometry seen in figure 3.14a is simulated. Therefore, the symmetry boundaries can be removed. The left and right WG after the splitter are referred to as WG2L and WG2R respectively, as seen in figure 3.20.

The splitter efficiency is evaluated by comparing the total energy ratio of WG2L and WG2R with respect to their combined total energy. An ideal 50-50 splitter would result in a ratio of 50% for both WG2L and WG2R.

3.6.2. Amplitude measurement

To evaluate if the out-of-plane wave displacement is large enough to overcome the measuring limit of $15pm$, a line displacement calculation is added to the complete hexagonal splitter simulation. This is done by introducing a 2D cutline data set along the center lines of WG1, WG2L and WG2R. A 1D plot featuring a line graph is then made using this cutline. The resulting plot data is exported to MATLAB. To visualize the measuring limit, a dotted line at $y = 15pm$ is added.

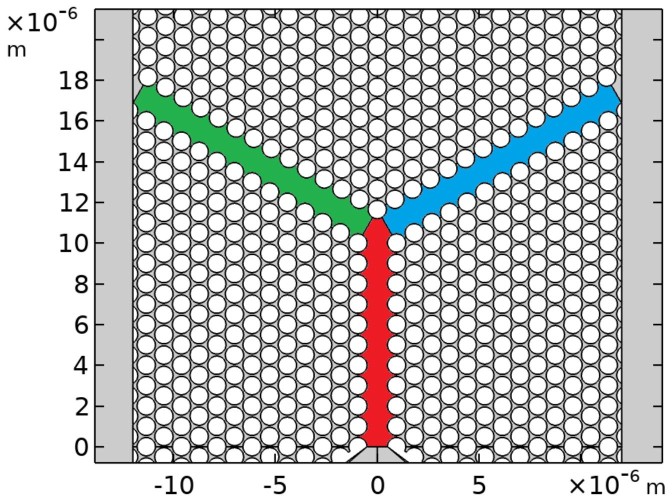

Figure 3.20: Selection for the complete splitter WG domains. (red) WG1. (green) WG2L. (blue) WG2R.

4
Results

This chapter contains the results of the simulations and analysis discussed in the previous chapter. First, the bandstructures of the simulated hexagonal and square lattices are presented. The found bandgaps are illustrated and their corresponding BG% are given. Next, the results of the different design parameter simulations are given. These include the excitation methods, excitation frequency influence, acoustic beam splitters and the complete splitter simulation. The total energy graphs for each highest confining design parameter is shown together with a visual of the wave motion at certain time steps. Finally, the splitter efficiency and observed wave amplitudes are presented.

4.1. Hexagonal and Square Lattice Bandstructures

Here, the results of the eigenfrequency study performed in section 3.2.3 are shown. The hexagonal lattice bandstructure is shown in figure 4.2. The bandstructure contained three bandgaps in the GHz range. The bandgap around $f_{mid} = 2.925GHz$ achieved the highest BG% of 57.3%. The observed values of the hexagonal lattice bandgaps and their BG%'s are shown in table 4.1.

The square lattice bandstructure is shown in figure 4.3. A bandgap is detected around $f_{mid} = 3.200GHz$ with a BG% of 37.5%. In table 4.2, the frequency values for the BG% calculation are shown.

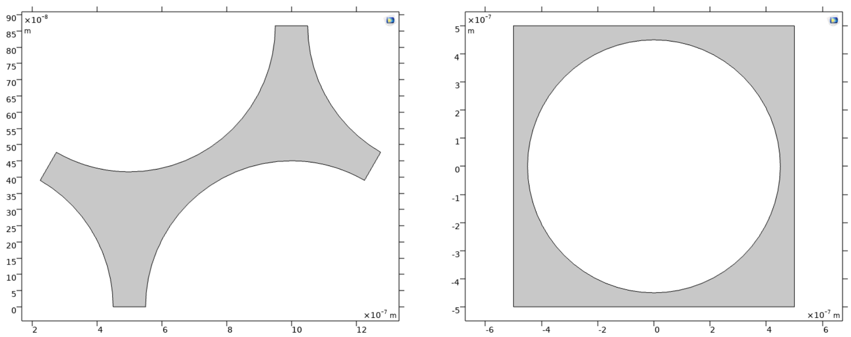

(a) (b)

Figure 4.1: The simulated unit cells for the (a) hexagonal and (b) square lattice bandstructures.

Table 4.1: Hexagonal lattice bandgaps and the frequencies needed to calculate the BG%.

	$f_{bottom}[GHz]$	$f_{top}[GHz]$	$f_{mid}[GHz]$	$\Delta f[GHz]$	$BG\%$
1st Bandgap	2.100	3.750	2.925	1.650	57.3%
2nd Bandgap	5.300	5.750	5.525	0.450	8.8%
3rd Bandgap	7.000	9.350	8.175	2.350	29.0%

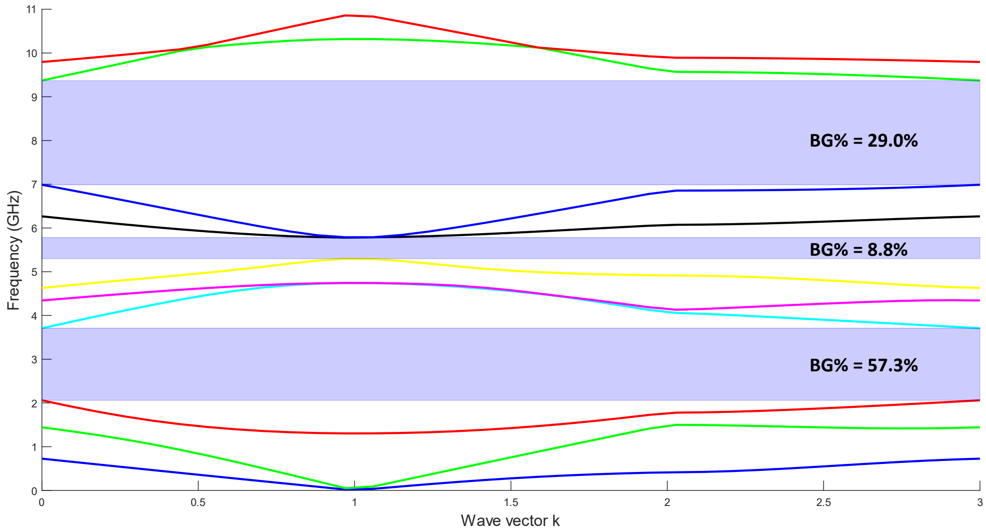

Figure 4.2: Hexagonal lattice bandstructure containing three bandgaps in the GHz range (blue shaded areas).

Table 4.2: Square lattice bandgap and the frequencies needed to calculate the BG%.

	$f_{bottom}[GHz]$	$f_{top}[GHz]$	$f_{mid}[GHz]$	$\Delta f[GHz]$	$BG\%$
1st Bandgap	2.600	3.800	3.200	1.200	37.5%

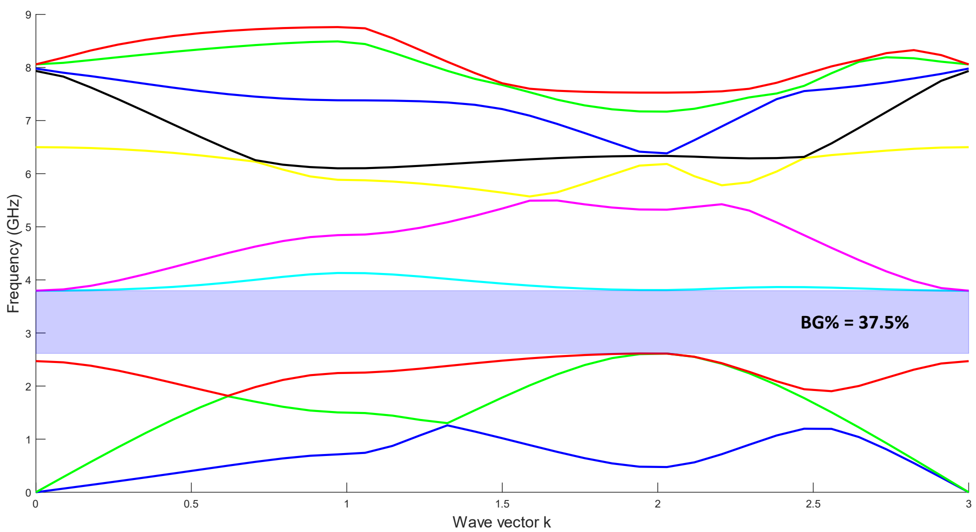

Figure 4.3: Square lattice bandstructure containing a GHz bandgap (blue shaded area).

4.2. Straight Waveguide Excitation Methods

When simulating an elastic wave excited inside the WG, it was observed that a spot excitation located at (0, 0.5a) resulted in a wave confinement of 51.22%. For the simulations of a spot located at (0, 0) or a plane wave excitation at (0, 0), the confinements were lower. The confinement values are shown in table 4.3. The total energy graph of the (0, 0.5a) spot excitation can be seen in figure 4.4.

Table 4.3: WG wave confinements for the different spot excitation methods.

	Spot (0, 0)	Spot (0, 0.5a)	Plane wave (0, 0)
WG wave confinement	49.79%	51.22%	46.22%

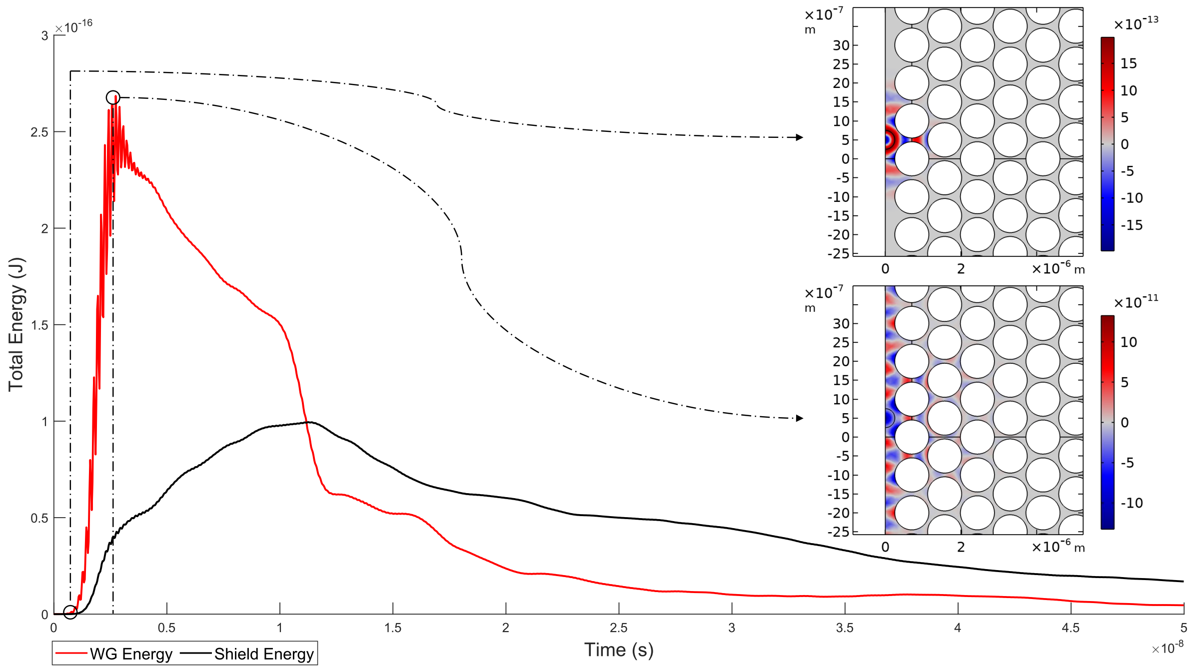

Figure 4.4: Total energy: Spot excitation at (0, 0.5a). The inserts display the out-of-plane wave motion [m]. (top) Start of the circular spot excitation ($t = 4.4 * 10^{-10} s$). (bottom) Maximum observed total energy inside the WG ($t = 3.8 * 10^{-9} s$).

For excitations that use a coupling wedge with a plane wave assumption, it was observed that a coupling wedge with a 4x3 shape ratio resulted in the highest wave confinement of 82.10%. All simulated coupling wedge shape confinement ratio's can be seen in table 4.4. They all showed a higher confinement ratio than the excitations done inside the WG. The total energy graphs of the 4x3 wedge are displayed in figure 4.5 and figure 4.6.

Table 4.4: WG wave confinements for the different wedge excitation methods.

	0x3 Wedge	1x3 Wedge	2x3 Wedge	3x3 Wedge	4x3 Wedge	5x3 Wedge
WG wave confinement	72.06%	70.58%	75.36%	81.38%	82.10%	79.06%

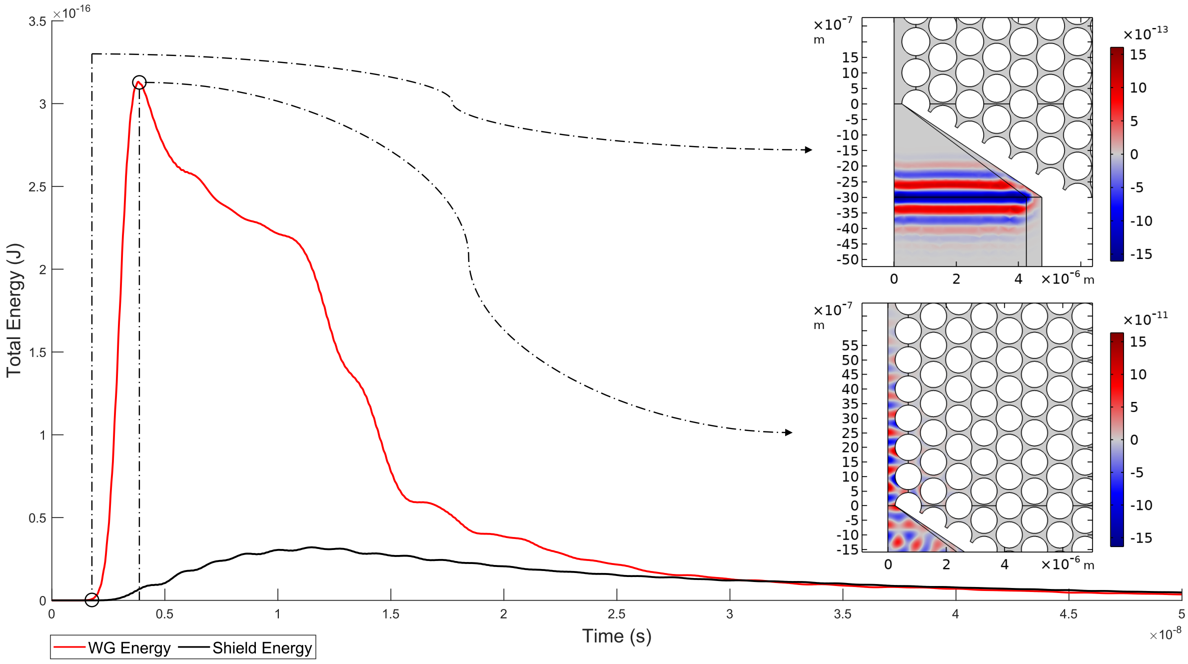

Figure 4.5: Total Energy: 4x3 Wedge excitation. The inserts display the out-of-plane wave motion [m]. (top) Beginning of the plane wave excitation inside the coupling wedge ($t = 3.0 * 10^{-10} s$). (bottom) Maximum observed total energy inside the WG ($t = 3.8 * 10^{-9} s$).

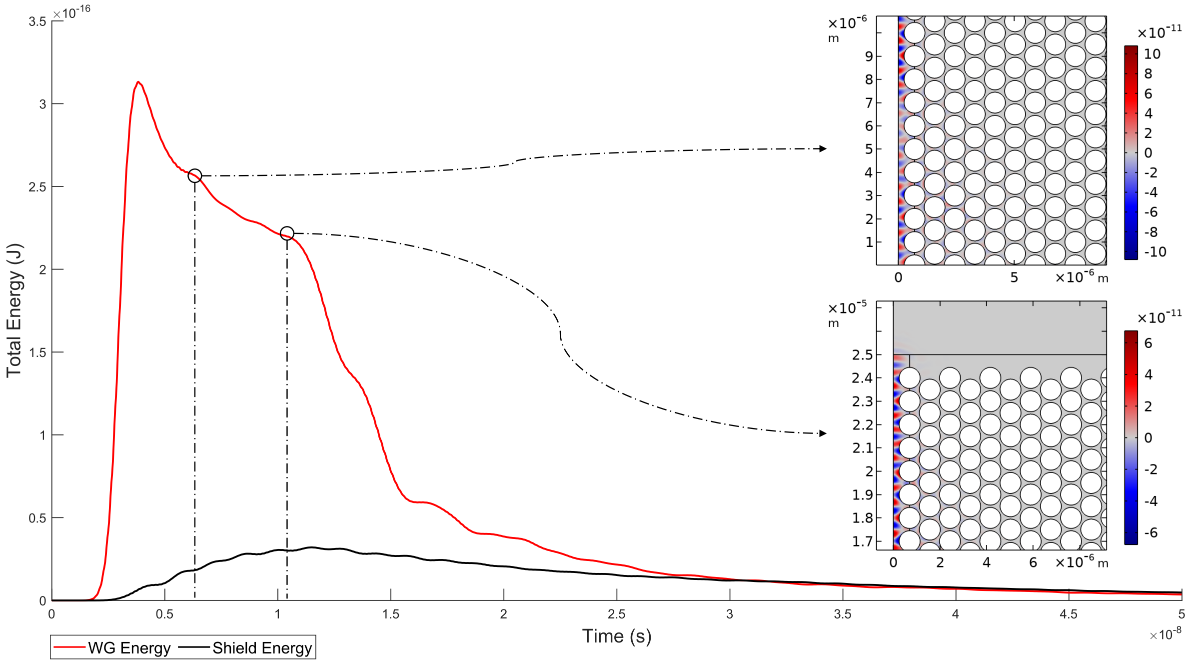

Figure 4.6: Total Energy: 4x3 Wedge excitation. The inserts display the out-of-plane wave motion [m]. (top) Observed fluctuation in the decreasing rate of total energy ($t = 6.30 * 10^{-9} s$). (bottom) Wave reaches the WG end ($t = 1.02 * 10^{-8} s$).

4.3. Excitation frequency influence

For the hexagonal lattice straight WG design that was used, it was observed that a frequency of $2.925GHz$ produced the highest confinement ratio of 82.09%. The $3.250GHz$ excitation, which has its frequency domain peak in the center of the 1st bandgap, a confinement ratio of 81.82% was achieved. The total energy graphs of both the $2.925GHz$ and $3.250GHz$ excitation are shown in figure 4.7. The confinement ratio of the $3.250GHz$ excitation is higher than that of the $2.925GHz$ excitation until $t = 1 * 10^{-8}s$, namely 93.41% versus 93.32%. The confinement ratio's of the studied frequencies are shown in table 4.5.

An excitation frequency that lays outside of the bandgap was found to have a lower confinement ratio. For $1.000GHz$, the confinement resulted in 11.09%. The total energy graphs for the $1.000GHz$ excitation are presented in figure 4.8 and figure 4.9.

Table 4.5: WG wave confinements for different frequencies inside the 1st hexagonal bandgap.

	$2.450GHz$	$2.925GHz$	$3.250GHz$	$3.975GHz$
WG wave confinement	60.63%	82.09%	81.82%	78.76%

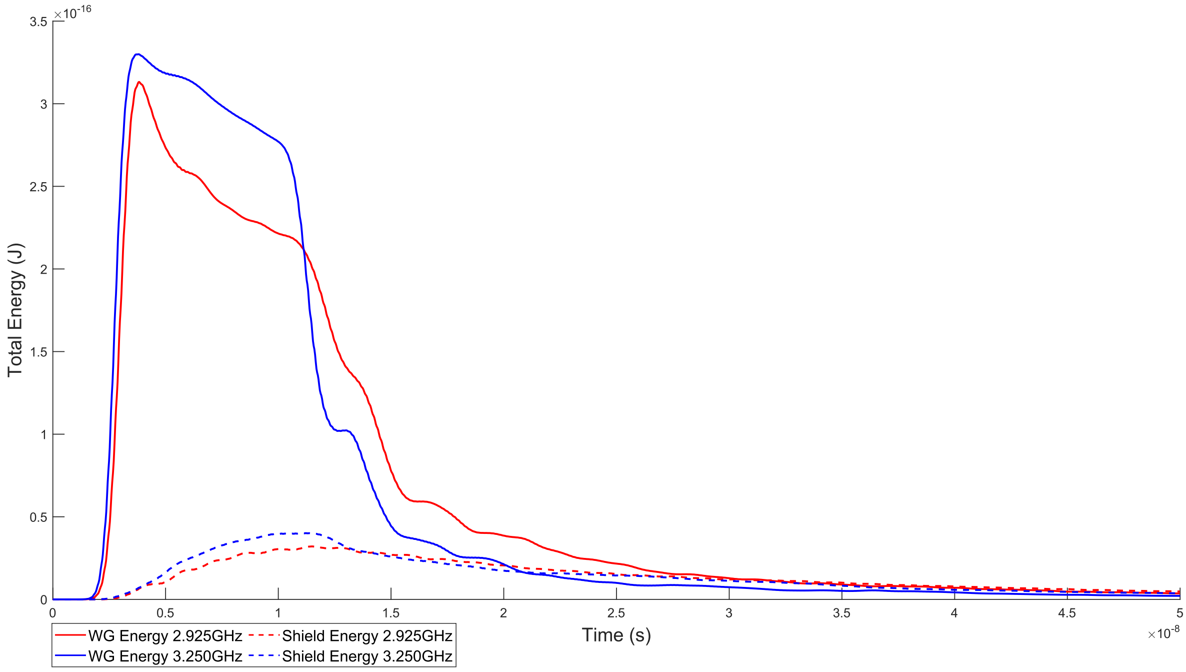

Figure 4.7: Total Energy: 2.925 and 3.250 GHz.

Table 4.6: WG wave confinement using a frequency outside the bandgap.

	$1.000GHz$
WG wave confinement	11.09%

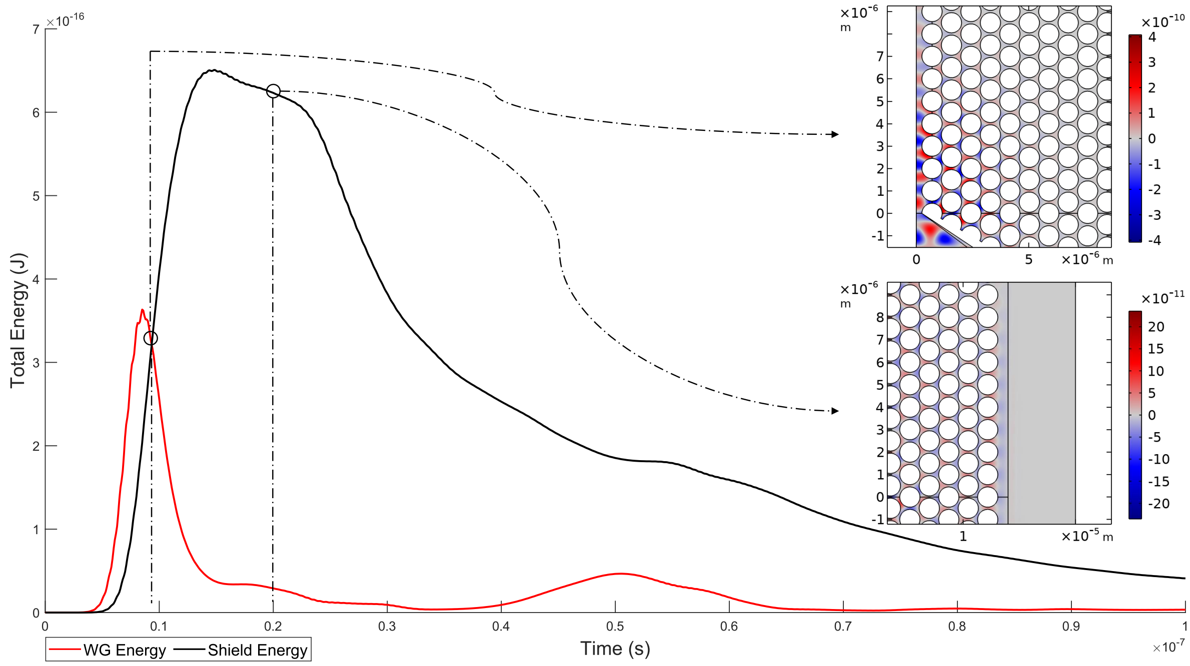

Figure 4.8: Total Energy: 1.000 GHz. The inserts display the out-of-plane wave motion [m]. (top, $t = 9.5 * 10^{-9} s$) Total energy inside the Shield becomes higher than the total WG energy. (bottom, $t = 2.0 * 10^{-8} s$) Wave traveled through the Shield and reaches the absorbing domain.

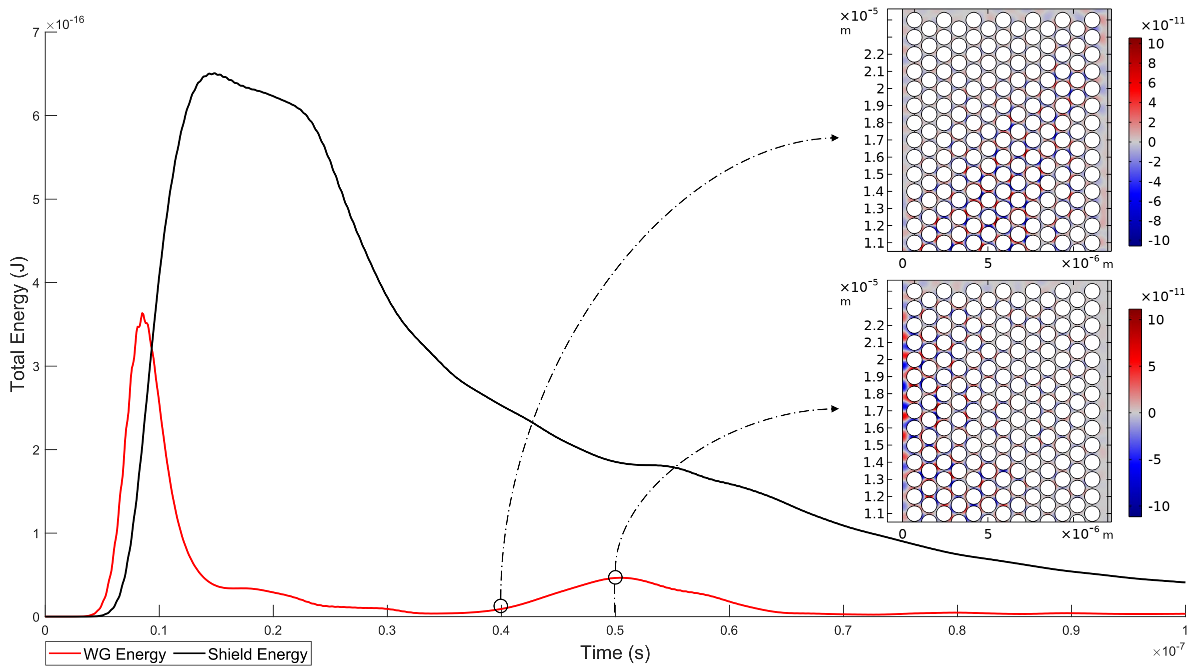

Figure 4.9: Total Energy: $1.000 GHz$. The inserts display the out-of-plane wave motion [m]. (top, $t = 4.0 * 10^{-8} s$) Wave reentered the WG domain, increasing the total WG energy. (bottom, $t = 5.0 * 10^{-8} s$) Total energy inside the WG reaches a second maximum.

4.4. Acoustic Beam Splitters

4.4.1. Hexagonal Lattice Splitter

The hexagonal lattice splitter design with a WG width of $1.00a$ achieved a wave confinement of 85.03%. This was the highest out of the four simulated WG widths, whose values are given in table 4.7. The total energy graph of the $1.00a$ hexagonal splitter, where the energies for WG1 and WG2 are combined, is shown in figure 4.10.

Figure 4.11 and figure 4.12 display total energy graphs of the $1.00a$ hexagonal splitter with separate values for WG1 and WG2.

Table 4.7: WG wave confinements for the hexagonal lattice splitters.

	$0.50a$	$0.75a$	$1.00a$	$1.25a$
WG wave confinement	73.20%	76.18%	85.03%	76.21%

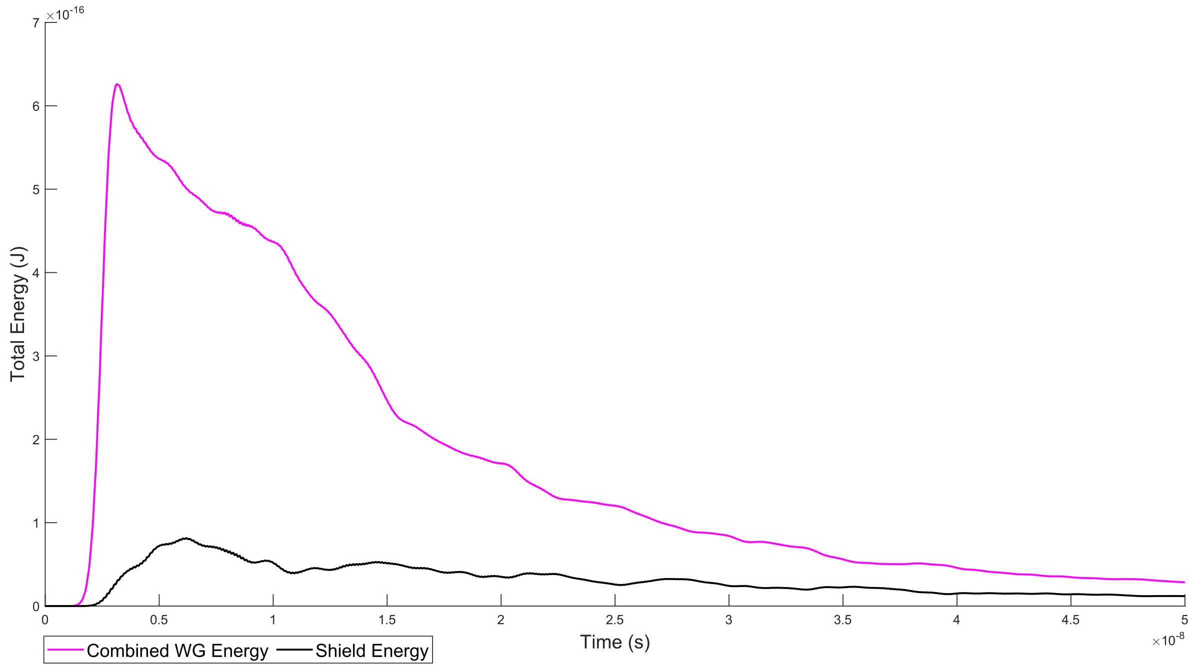

Figure 4.10: Total Energy: hexagonal splitter ($1.00a$) with combined energies of WG1 and WG2.

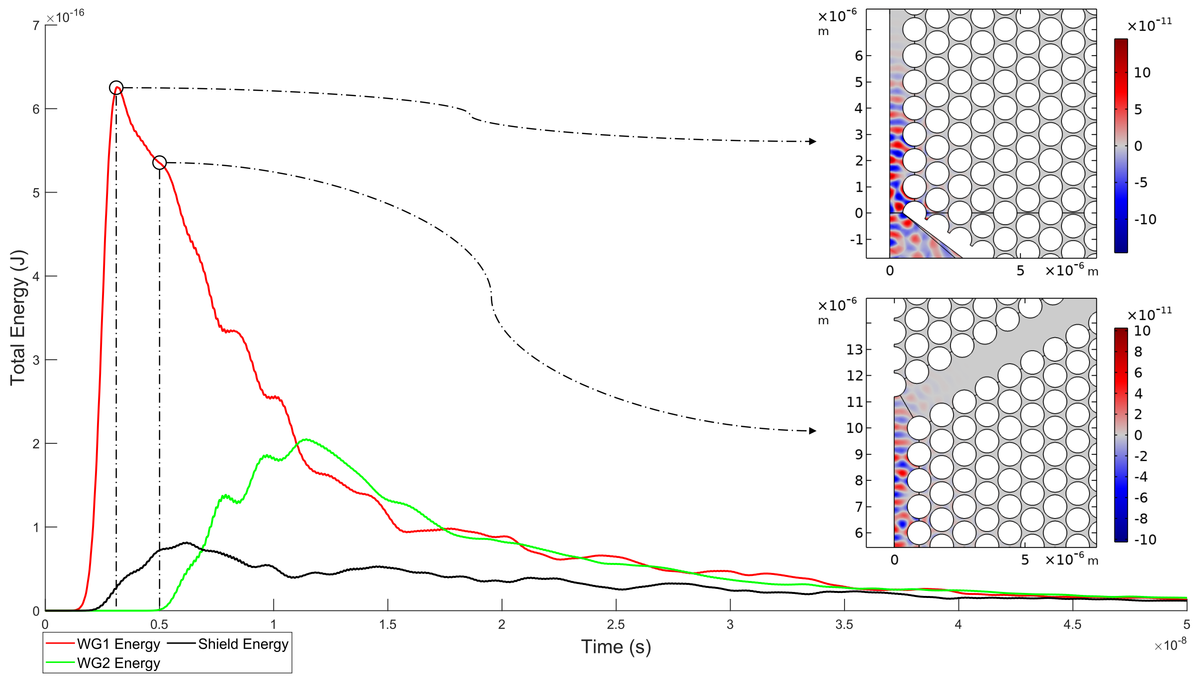

Figure 4.11: Total Energy: hexagonal splitter ($1.00a$). The inserts display the out-of-plane wave motion [m]. (top, $t = 3.2 * 10^{-9}s$) Maximum total WG1 energy . (bottom, $t = 5.0 * 10^{-9}s$) Wave reaches the splitter and enters the WG2 domain.

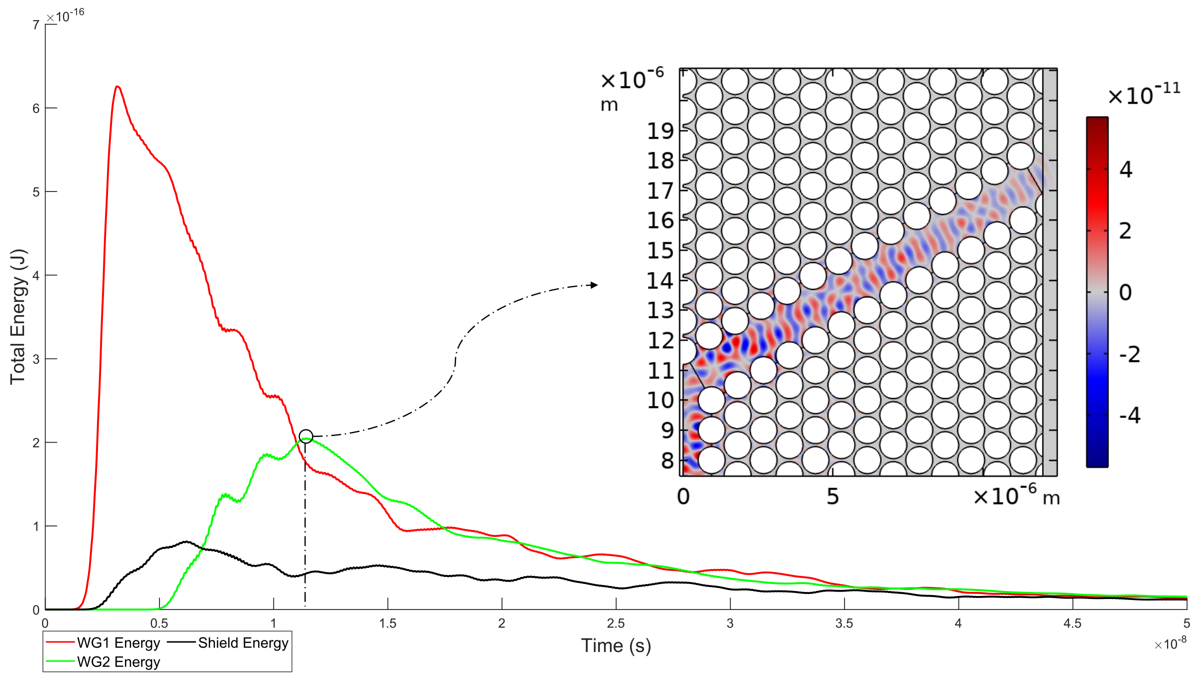

Figure 4.12: Total Energy: hexagonal splitter ($1.00a$). The insert displays the out-of-plane wave motion [m] at $t = 1.14 * 10^{-8}s$. Here, the total WG2 energy reaches a maximum as the wave leaves the WG domain.

4.4.2. Square Lattice Splitter

For the square lattice splitter, it was observed that a WG width of $1.00a$ produced the highest wave confinement of 51.10%. The other WG widths achieved lower wave confinements, comparable to the hexagonal lattice splitter observations. All confinement ratio's are seen in table 4.8. The total energy graph of the 1.00a square splitter, where the energies for WG1 and WG2 are combined, is shown in figure 4.13.

Figure 4.14 and figure 4.15 display total energy graphs of the 1.00a square splitter with separate values for WG1 and WG2.

Table 4.8: WG wave confinements for the square lattice splitters.

	$0.50a$	$0.75a$	$1.00a$	$1.25a$
WG wave confinement	49.77%	47.28%	51.10%	46.65%

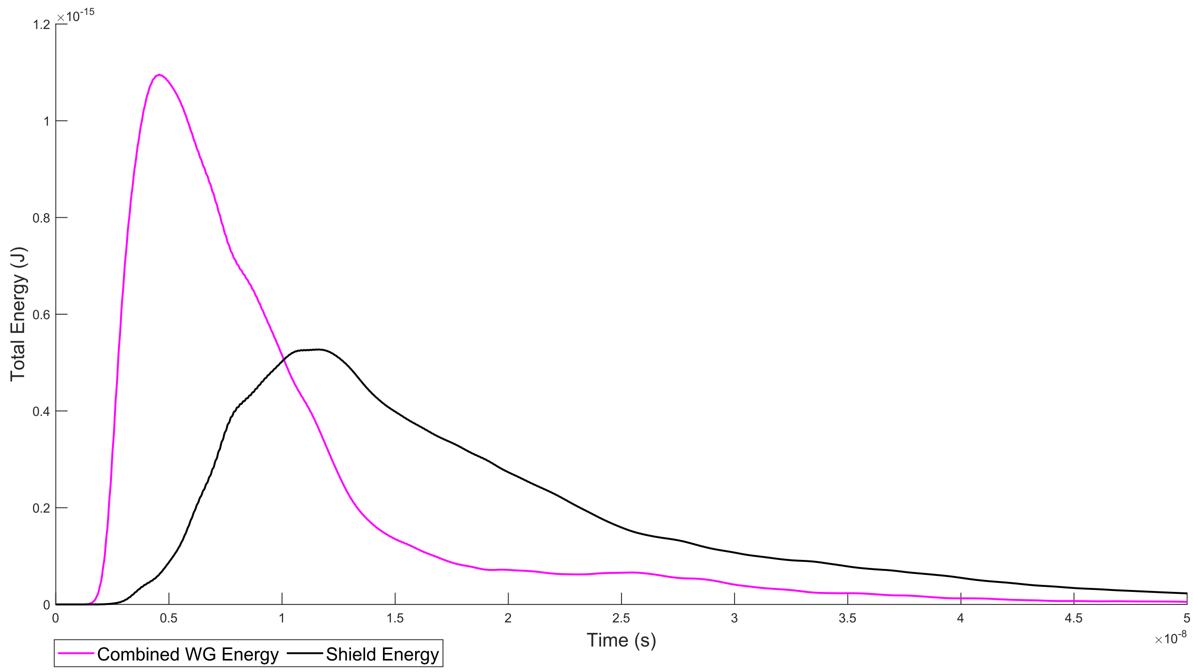

Figure 4.13: Total Energy: square splitter (1.00a) with combined energies of WG1 and WG2.

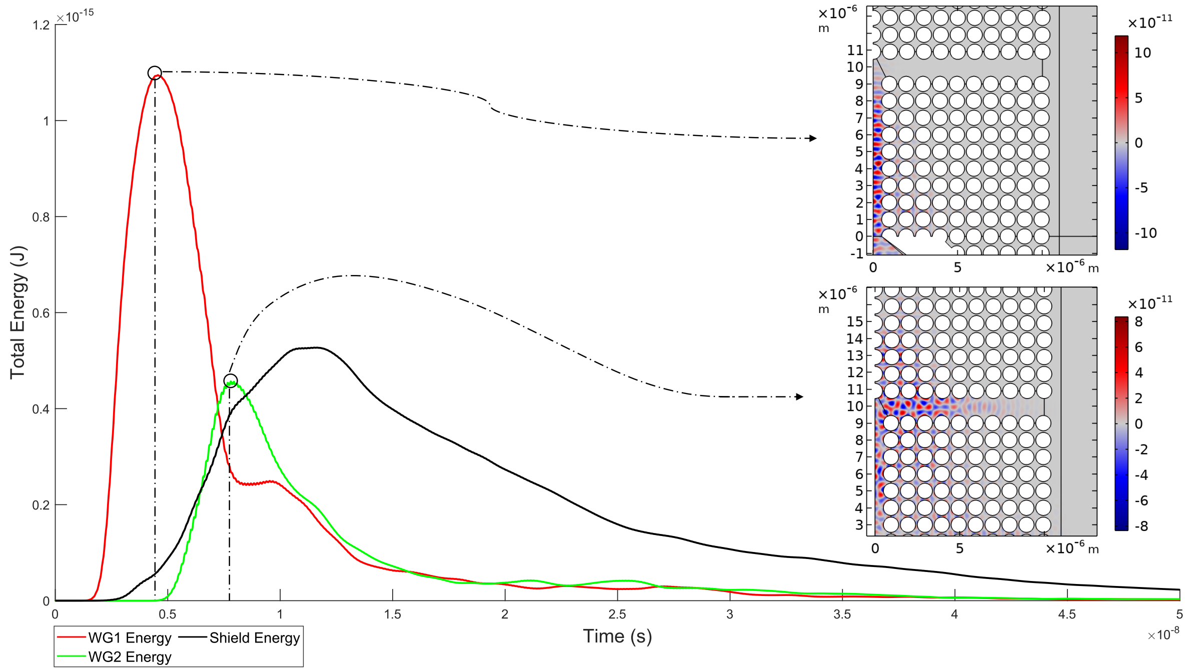

Figure 4.14: Total Energy: square splitter $(1.00a)$. The inserts display the out-of-plane wave motion [m]. (top, $t = 4.5 * 10^{-9}s$) Total WG1 energy maximum. (bottom, $t = 7.9 * 10^{-9}s$) Total WG2 energy maximum.

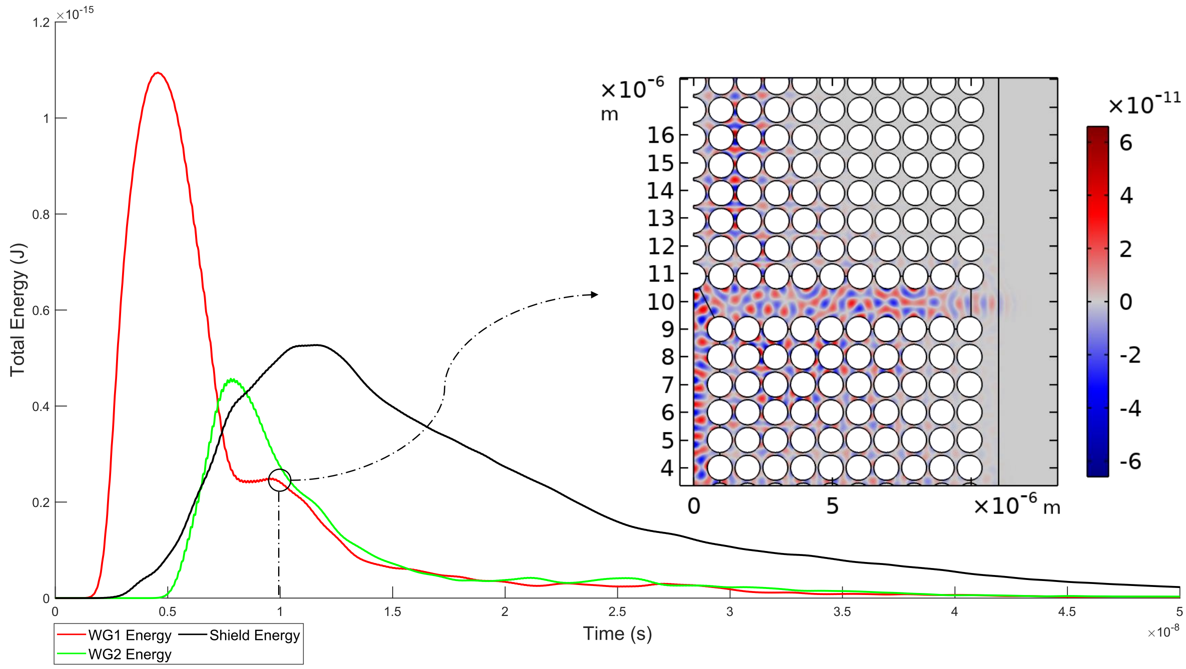

Figure 4.15: Total Energy: square splitter $(1.00a)$. The insert displays the out-of-plane motion [m] at $t = 1.0 * 10^{-8}s$. Here, the wave reaches the end of the WG domain and enters the absorbing domain.

4.4.3. Complete Hexagonal Lattice Splitter

The complete hexagonal lattice splitter achieved a wave confinement of 85.03%. This is the same wave confinement as that was found for the the hexagonal splitter simulation that used the symmetry boundary conditions. The total energy graph of the complete hexagonal splitter, where the energies for WG1, WG2R and WG2L are combined, is shown in figure 4.16. Figure 4.17 and figure 4.18 display total energy graphs of the complete Hexagonal splitter with separate values for WG1, WG2R and WG2L.

The splitter efficiency ratio's are shown in table 4.9.

Figure 4.19 displays the wave amplitude measurements of the complete Hexagonal splitter. The observed wave amplitude was above $15pm$ at the end of both WG2R and WG2L.

Table 4.9: Total energies of the complete hexagonal splitter domains.

	WG2	WG2R	WG2L
Total Energy (J)	$5.92 * 10^{-24}$	$2.96 * 10^{-24}$	$2.96 * 10^{-24}$
Percentage of WG2 (%)	-	50%	50%

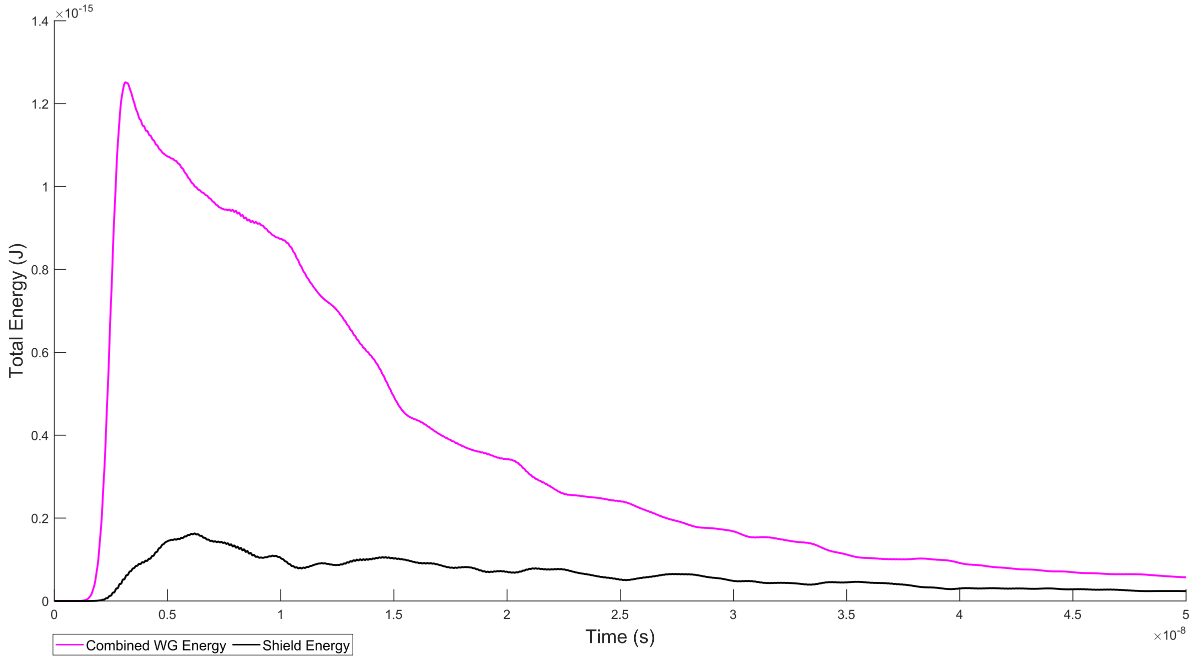

Figure 4.16: Total Energy: Complete hexagonal splitter with combined energies of WG1 and WG2.

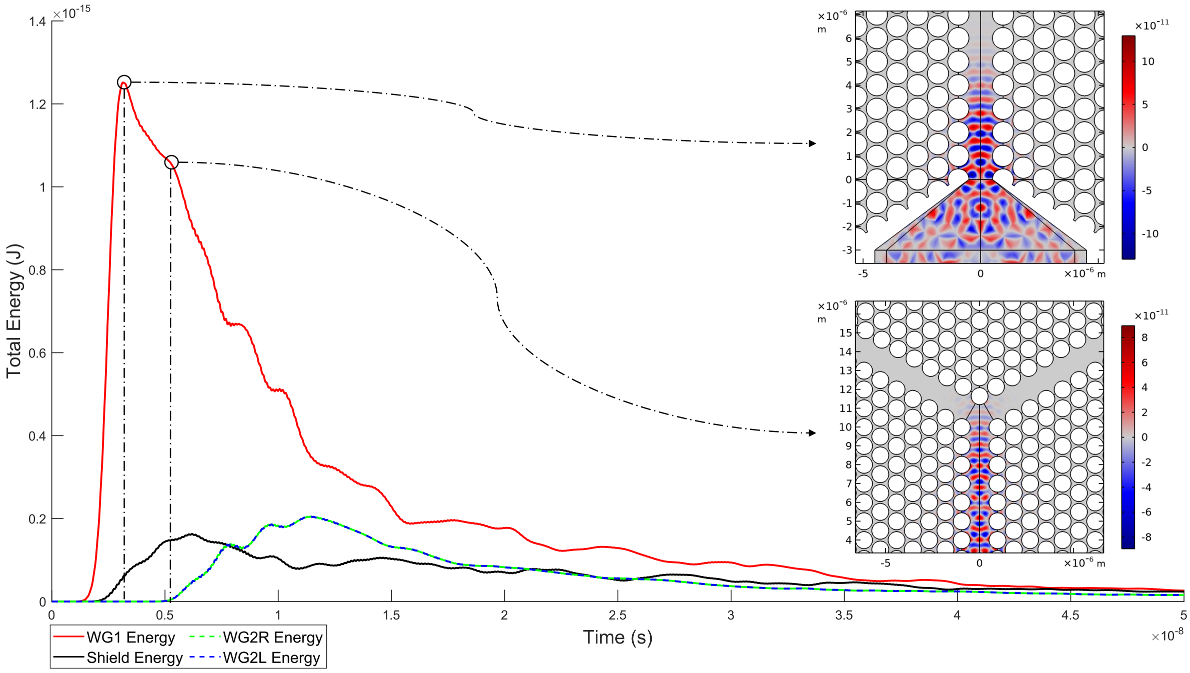

Figure 4.17: Total Energy: Complete hexagonal splitter. The inserts display the out-of-plane wave motion [m]. (top, $t = 3.0 * 10^{-9}s$) Maximum total WG1 energy. (bottom, $t = 5.0 * 10^{-9}s$) Wave reaches the splitter and enters the domains of WG2R and WG2L.

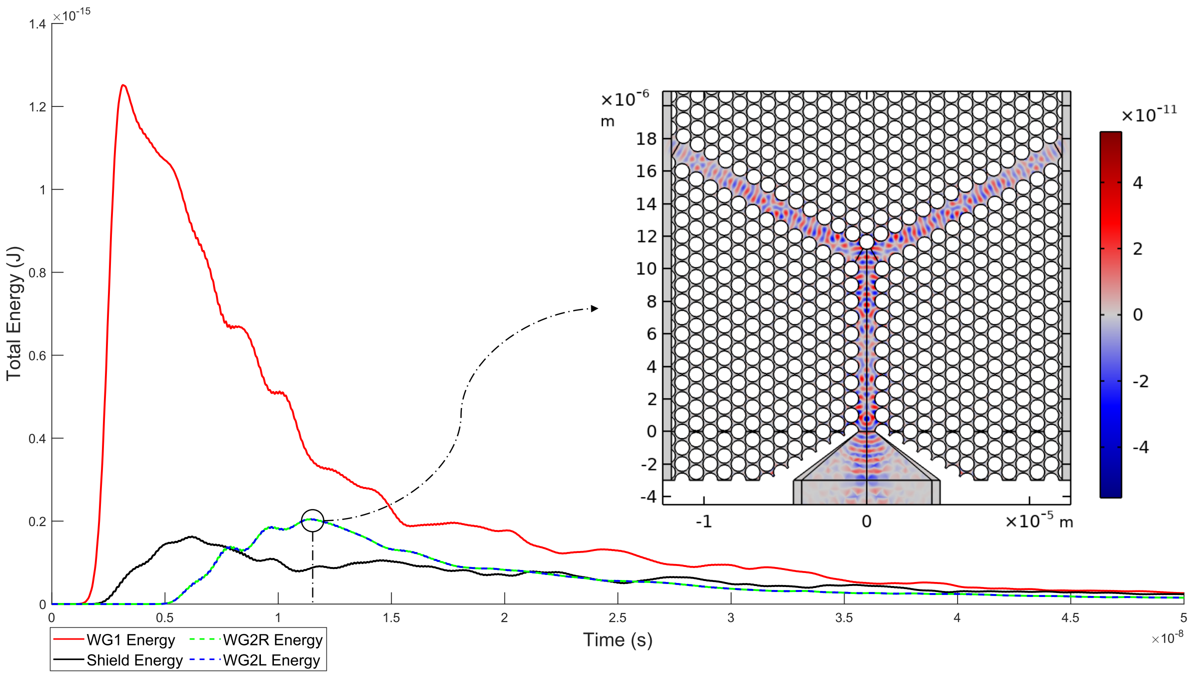

Figure 4.18: Total Energy: Complete hexagonal splitter. The insert displays the out-of-plane motion [m] at $t = 1.14 * 10^{-8}s$. Here, a maximum of the total energy for WG2R and WG2L is observed as the wave enters the absorbing domain.

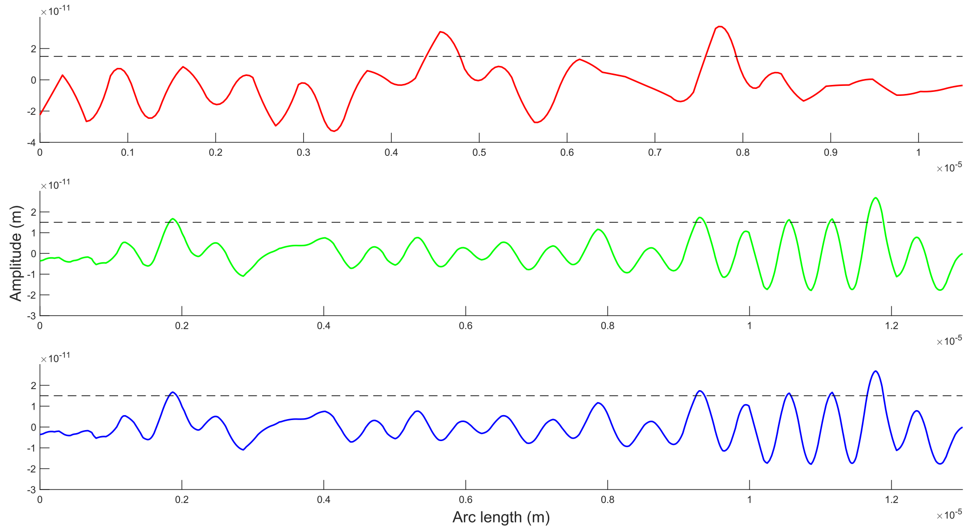

Figure 4.19: Complete hexagonal splitter wave amplitude at $t = 1.58 * 10^{-8}$. (red) WG1. (green) WG2R. (blue) WG2L. The black dashed line indicates the measuring limit of $15pm$.

5 Discussion

5.1. Determining the bandgap frequencies

The bandstructures found in this study are assumed to be ideal. This means that the upper and lower limits of the eigenfrequencies are directly taken from the calculations made by COMSOL. In reality, the wave transmission through the PnC can become zero but the measured transmission will never reach zero due to measurement noise. A threshold for this measurement noise is needed to overcome this issue.

5.2. Total energy flat lines

Figure 4.17 shows the total energy graph of the complete hexagonal splitter, it can be seen that around $t = 8 * 10^{-9}s$ and $t = 10 * 10^{-9}s$ the total energy remains constant for a short period before continuing to decrease.

A possible explanation for this behaviour is reflecting waves traveling along the edge of the WG1 and WG2 boundaries. Thereby keeping the total energy in the specific domain constant before reflecting and changing the propagation direction. By measuring the duration of this period and comparing it to the travel time of the wave across this edge, it is possible to test this theory.

The edge length is $1.00a = 1.0 * 10^{-6}m$. The wave envelope speed (group velocity) is found to be $2.2*10^{3}m/s$. This is lower than the pressure or shear wave speed of the material. This can happen if the group wave velocity is lower than the phase velocity. This means that the envelope of the elastic wave is traveling slower than the frequency speed component (phase velocity). Dividing the edge length by the wave speed, a period of $1.0 * 10^{-6}/2.2 * 10^{3} = 4.5 * 10^{-10}$ would be expected. From the plots, it is observed that these periods are around $5.0 * 10^{-10}$. These periods are comparable and therefore the assumption of reflecting waves traveling along the domain boundaries is found to be plausible.

5.3. Two travelling waves

In some simulations, it was noticed that there was a second pulse wave present behind the initial pulse wave. This second pulse wave may originate from a reflecting wave coming from the backside of the coupling wedge.

By simulating a coupling wedge twice as long along the y-direction, it was found that the second traveling wave disappeared. Surprisingly, the wave confinement decreased in this simulation. Since this second wave would travel a longer distance than the initial pulse, it is possible that the second pulse increased the wave confinement because of a higher plane wave resembling. This second wave possessing an increased plane wave characteristic would travel along the WG more smoothly, increasing the wave confinement. Therefore, by removing this second wave the confinement decreases.

5.4. Membrane thickness

In this study, the membrane thickness is kept at a constant of $80nm$. Future investigations will have to establish the influence of the membrane thickness on the wave confinement and propagation distance. A thicker membrane could result in higher intrinsic losses, possibly lowering both confinement and propagation. A thinner membrane would lower the needed energy to construct the vibrations. However, this could cause the shield to vibrate more easily and thus lower the wave confinement.

5.5. Gold excitation trial

SiN is not the expected optimal material for phonon generation by a pulsed laser. This is due to the relatively low light absorption coefficient ($\alpha = 2.42cm^{-1}$ [21]) of SiN. The light absorption can be increased by printing a layer of gold ($\alpha = 8.72 * 10^5 cm^{-1}$ [17]) on top of the SiN.

To study the effects of adding this gold material, the simulation of the hexagonal splitter is altered by adding a gold circle inside the coupling wedge. The prescribed velocity is set on the newly introduced gold circular boundary. It was found that the confinement ratio was higher than the original hexagonal splitter simulation, with the gold simulation reaching 85.4% confinement. However, the total energy levels were lower than the SiN plane wave excitation and the confinement in WG2 was also lower. This resulted in similar out-of-plane displacements for WG2 and the PnC shield.

5.6. Ideal splitter meshing

The splitter produces an ideal 50-50 splitting of energy.

A symmetric mesh is important for this results. If not a $50 - 50$ is reached, changes are that the mesh is either not symmetric or to large at the splitter point. A small enough mesh would probably result in a near $50 - 50$ splitter regardless of being perfect symmetric because of the smaller variances in mesh element sizes. However, this would obviously increase the computational time unnecessarily, since there exists a prescribed maximum mesh size for elastic waves. If no symmetric node is added for the mesh in the symmetric boundaries, COMSOL tries to make the best fit for the maximum element size, this will not always result in a perfect symmetric meshing.

The automatic COMSOL mesh resulted in a 48.5% $-$ 51.5% splitter.

5.7. Amplitude detection

The results of the amplitude measurement show that an initial excitation amplitude of $2m/s$ barely reaches the measuring limit of $15pm$.

An additional simulation with an increased initial excitation amplitude of $10m/s$ resulted in observed amplitudes at the end of WG2 of around $120pm$.

It is found that the wave confinement is not influenced by the excitation power. Thus, an increase in excitation power can help with wave detection without influencing the wave confinement.

6 Conclusion

In this study, multiple designs for suspended SiN GHz acoustic beam splitters operating at room temperature have been investigated. By systematically examining the influence of the design parameters, the splitter design that achieves the highest wave confinement was established. This was done with the use of the FEM solver COMSOL Multiphysics in combination with the computing platform MATLAB.

The Eigenfrequency study resulted in both hexagonal and square lattice bandstructures showing full bandgaps in the GHz range. The 1st hexagonal bandgap possessed the highest BG% of 57.3% centered around $f_{mid} = 2.925GHz$.

Multiple wave excitation methods were simulated and studied. From these simulations, it can be concluded that an excitation outside of the WG, using a 4x3 coupling wedge with a plane wave assumption, achieves the highest wave confinement.

Due to the simulated pulsed laser excitation, it was necessary to evaluate the FFT of the Gaussian sine pulses. The wave confinement is maximized when the high frequency Gaussian peak in the frequency domain is located in the centre of the bandgap region.

As expected, the wave confinement was lower when the frequency domain peaks of the excitation were located outside of the bandgap.

For both the hexagonal and square lattices, splitter designs were made with the WGs located along the symmetry axis of the used lattices. It was found that a WG width of $1.00a$ produced the highest wave confinement for both lattices. Showing similar results to PnC devices found in the literature [35] [23] [45] [30] [28]. The hexagonal splitter achieved the overall highest confinement of 85.03%.

The computational limits required the simulations to be done with the use of a symmetry boundary. This meant half of the geometry was simulated which reduced the computation time. Once the optimal splitter design was found, a full geometry simulation was done to study the effect of the symmetry boundary. It can be concluded that the symmetry boundary gives the same results as the complete geometry. The wave confinement of the complete simulated hexagonal splitter stayed at 85.03%. The complete geometry simulation enabled the analysis of the splitter's efficiency regarding the ratio of total energy in the WG2 domains. This analysis showed that the hexagonal splitter achieves a $50\% - 50\%$ splitting ratio when using a symmetric mesh.

The wave amplitude measurement showed a displacement greater than $15pm$ at the end of both WG2 domains with an initial wave amplitude of $2m/s$. This demonstrated a wave propagation distance of 23 lattice constants, equivalent to the total WG length, in the complete hexagonal splitter. Thereby achieving and surpassing the device requirement of a minimum wave propagation distance of 20 lattice constants.

By studying the effects of certain design parameters, this numerical study can conclude that PnCs fabricated in suspended high stress SiN membranes are a promising solution for on-chip GHz out-of-plane acoustic beam splitters operating at room temperature. It can also conclude that the hexagonal lattice splitter designs achieve higher wave confinement compared to the square lattice splitter designs.

Acknowledgements

First of all, I want to thank Dr. G.J. Verbiest and Dr. R.A. Norte for their support during my Master's Thesis. I have learned a lot from them during my thesis project. I got to learn about many interesting subjects of which some were completely new to me. They taught me how to perform a scientific research project and how important it is to be critical of your own work. Our weekly meetings meant we had frequent contact which I found helpful.

Next, I want to thank all the members of the Norte research group. During the weekly group meetings, I was able to ask questions and present my issues regarding my simulations or other general topics which was helpful for continuing my project. It was interesting to get an insight into one of these research groups and I enjoyed being a part of one.

I am glad to say that the project will be continued and my research will be tested experimentally. I am looking forward to the results and want to wish András success in experimentally reproducing the findings of my designs and research in the lab.

Finally, I want to thank my friends and family for supporting me throughout my study. They always kept me motivated and helped me where they could.

M.C.C.Y. van der Vis
Delft, December 2022

References

[1] T.P.M. Alegre et al. “Quasi-two-dimensional optomechanical crystals with a complete phononic bandgap”. In: *Optics Express* 19 (2011). DOI: https://doi-org.tudelft.idm.oclc.org/10.1364/OE.19.005658.

[2] O.R. Bilal, C.H. Yee, and J. Rys. “Experimental realization of phonon demultiplexing in three-dimensions”. In: *Applied Physics Letters* 118 (2021). DOI: https://doi.org/10.1063/5.0030830.

[3] J.D. Clayton. “Dielectrics and Piezoelectricity”. In: *Solid Mechanics and Its Applications* 177 (2011). DOI: https://doi.org/10.1007/978-94-007-0350-6_10.

[4] T.J. Cui et al. “Information Metamaterial Systems”. In: *iscience* 23 (2020). DOI: https://doi.org/10.1016/j.isci.2020.101403.

[5] S. Dante et al. “All-optical phase modulation for integrated interferometric biosensors”. In: *Optics express* 20 (2012). DOI: 10.1364/OE.20.007195.

[6] The Editors of Encyclopaedia Britannica. *Principle types of seismic waves*. 2022. URL: https://www.britannica.com/science/earthquake-geology/Shallow-intermediate-and-deep-foci#/media/1/176199/210259.

[7] S.A. Fedorov et al. “Evidence for structural damping in a high-stress silicon nitride nanobeam and its implications for quantum optomechanics”. In: *Physics Letters A* 382 (2017). DOI: http://dx.doi.org/10.1016/j.physleta.2017.05.046.

[8] O. Florez et al. “Engineering nanoscale hypersonic phonon transport”. In: *Nature Nanotechnology* 17 (2022). DOI: https://doi.org/10.1038/s41565-022-01178-1.

[9] W. Fu et al. “Phononic integrated circuitry and spin–orbit interaction of phonons”. In: *Nature Communications* 10 (2019). DOI: https://doi.org/10.1038/s41467-019-10852-3.

[10] Z. Guo et al. “Subwavelength bandgap phononic crystals with mixed resonant modes”. In: *Physics Letters A* (438 2022). DOI: https://doi.org/10.1016/j.physleta.2022.12810.

[11] M.V. Gustafsson et al. “Propagating phonons coupled to an artificial atom”. In: *Science* 346 (2014). DOI: 10.1103/PhysRevLett.116.147202.

[12] K.Y. Hashimoto. “Surface Acoustic Wave Devices in Telecommunications”. In: Springer, 2000, pp. 1–23. DOI: https://doi-org.tudelft.idm.oclc.org/10.1007/978-3-662-04223-6_1.

[13] D. Hatanaka et al. “Phonon waveguides for electromechanical circuits”. In: *Nature Nanotechnology* 9 (2014). DOI: https://doi-org.tudelft.idm.oclc.org/10.1038/nnano.2014.107.

[14] M.H. Jensen. *Introduction to the Elastic Waves, Time Explicit Interface*. 2020.

[15] M.H. Jensen. *Simulating Elastic Waves in the Time Domain Using COMSOL*. 2020.

[16] S. Jiang, H. Hu, and V. Laude. “Low-frequency band gap in cross-like holey phononic crystal strip”. In: *Journal of Physics D: Applied Physics* 151 (4 2018), p. 45601. URL: https://hal.archives-ouvertes.fr/hal-02131465.

[17] P. B. Johnson and R. W. Christy. “Optical Constants of the Noble Metals”. In: *Physics Review B* 6 (1972), pp. 4370–4379. DOI: 10.1103/PhysRevB.6.4370.

[18] M. Kalaee et al. “Quantum electromechanics of a hypersonic crystal”. In: *Nature Nanotechnology* 14 (2019). DOI: https://doi.org/10.1038/s41565-019-0377-2.

[19] O.A. Kaya et al. “Acoustic Mach–Zehnder interferometer utilizing self-collimated beams in a two-dimensional phononic crystal”. In: *Sensors and Actuators B: Chemical* (2014), pp. 197–203. DOI: ttp://dx.doi.org/10.1016/j.snb.2014.06.097.

[20] A. Khelif et al. “Guiding and bending of acoustic waves in highly confined phononic crystal waveguides”. In: *American Institute of Physics* 84 (2004). DOI: 10.1063/1.1757642.

[21] J. Kischkat et al. “Mid-infrared optical properties of thin films of aluminum oxide, titanium dioxide, silicon dioxide, aluminum nitride, and silicon nitride”. In: *Applied Optics* 51 (2012), pp. 6789–6798. DOI: https://doi-org.tudelft.idm.oclc.org/10.1364/AO.51.006789.

[22] E.P. Kosmidou, E.E. Kriezis, and T.D. Tsiboukis. “Analysis of tunable photonic crystal devices comprising liquid crystal materials as defects”. In: *IEEE Journal of Quantum Electronics* 41 (5 May 2005), pp. 657–665. DOI: 10.1109/JQE.2005.845925.

[23] M. Kurosu et al. “On-chip temporal focusing of elastic waves in a phononic crystal waveguide”. In: *Nature Communications* 9 (2018). DOI: 10.1038/s41467-018-03726-7.

[24] M. Lee et al. “Self-sealing complex oxide resonators”. In: *Nano Letters* 22 (2021). DOI: 10.1021/acs.nanolett.1c03498.

[25] M. Levine and C. White. “Material Damping Experiments at Cryogenic Temperatures”. In: (2003). DOI: http://dx.doi.org/10.1117/12.506838.

[26] B. Li et al. “Symmetrical 1×2 digital photonic splitting switch with low electrical power consumption in SiGe waveguides”. In: *Optical Society of America* 13 (2005).

[27] J. Li et al. “Acoustic beam splitting in two-dimensional phononic crystals using self-collimation effect”. In: *Journal of Applied Physics* 118 (2015). DOI: http://dx.doi.org/10.1063/1.4932138.

[28] G. Madiot et al. *Optomechanical generation of coherent GHz vibrations in a phononic waveguide*. 2022. DOI: https://doi.org/10.48550/arXiv.2206.06913.

[29] W. Magnus, F. Oberhettinger, and F.G. Tricomi. *Tables of Integral Transforms*. Vol. 1. McGRAW-HILL BOOK COMPANY, 1954.

[30] N.P. Mauranyapin et al. “Tunneling of Transverse Acoustic Waves on a Silicon Chip”. In: *Physical review applied* 15 (2021). DOI: http://dx.doi.org/10.1103/PhysRevApplied.15.054036.

[31] M. Melchiorri et al. “Propagation losses of silicon nitride waveguides in the near-infrared range”. In: *Applied Physics Letters* 86 (2005). DOI: https://doi-org.tudelft.idm.oclc.org/10.1063/1.1889242.

[32] M. Merschdorf. *Femtodynamics in Nanoparticles The Short Lives of Excited Electrons in Silver*. Fakultat fur Physik und Astronomie der Universitat Wurzburg, 2002.

[33] R.A. Norte, J.P Moura, and S. Gröblacher. “Mechanical Resonators for Quantum Optomechanics Experiments at Room Temperature”. In: *Physics Review Letters* 116 (2016). DOI: 10.1103/PhysRevLett.116.147202.

[34] D. Orive-Miguel et al. “Improving Localization of Deep Inclusions in Time-Resolved Diffuse Optical Tomography”. In: *Applied Sciences* (2020). DOI: 10.3390/app9245468ï. URL: www.mdpi.com/journal/applsci.

[35] R.N. Patel et al. “A single-mode phononic wire”. In: *Physical review letters* 121 (2017). DOI: DOI:10.1103/PhysRevLett.121.040501.

[36] C. Peng et al. “Experimental observations on material damping at cryogenic temperatures”. In: (2004). DOI: http://dx.doi.org/10.1117/12.561173.

[37] Phenomen. *All-Phononic circuits Enabled by Opto-mechanics*. 2020. DOI: https://doi.org/10.3030/713450.

[38] E. Rivet et al. “Constant-pressure sound waves in non-Hermitian disordered media”. In: *Nature Physics* 14 (2018). DOI: https://doi.org/10.1038/s41567-018-0188-7.

[39] scientificinquirer. *Meet the phonon, a low energy information carrier*. 2020.

[40] L. Shao et al. “Femtometer-amplitude imaging of coherent super high frequency vibrations in micromechanical resonators”. In: *Nature Communications* 13 (2022). DOI: https://doi.org/10.1038/s41467-022-28223-w.

[41] A. Shelke et al. “Wave guiding and wave modulation using phononic crystal defects”. In: *Intelligent Material Systems and Structures* 25 (2014). DOI: http://dx.doi.org/10.1177/1045389X13507344.

[42] D. Shin et al. “Spiderweb Nanomechanical Resonators via Bayesian Optimization Inspired by Nature and Guided by Machine Learning”. In: *Advanced Materials* 34 (2021). DOI: `https://doi.org/10.1002/adma.202106248`.

[43] Y. Tang et al. “One-way Acoustic Beam Splitter”. In: *Scientific reports* 8 (2018). DOI: `10.1038/s41598-018-29579-0`.

[44] A. Tavakoli et al. “Heat conduction measurements in ballistic 1D phonon waveguides indicate breakdown of the thermal conductance quantization”. In: *Nature Communications* 9 (2018). DOI: `DOI:10.1038/s41467-018-06791-0`.

[45] Y. Wang et al. “Hexagonal Boron Nitride Phononic Crystal Waveguides”. In: *ACS Photonics* 6 (2019). DOI: `http://dx.doi.org/10.1021/acsphotonics.9b01094`.

[46] Y.F. Wang et al. “Guiding and splitting Lamb waves in coupled-resonator elastic waveguides”. In: *Composite structures* 206 (2019). DOI: `10.1063/1.1757642`.

[47] N. Zen et al. “Engineering thermal conductance using a two-dimensional phononic crystal”. In: *Nature Communications* 5 (2014). DOI: `DOI:10.1038/ncomms4435`.

[48] C. Zhang, Q. Liu, and Z. Ouyang. “Band Gap Optimization for GHz Elastic Waves in Gold Phononic Crystals”. In: *IOP Conference Series: Materials Science and Engineering* 585 (1 2019). DOI: `10.1088/1757-899X/585/1/012051`.

[49] Z. Zhang et al. “An integrable and configurable phononic beam splitter based on self-collimated surface acoustic waves”. In: *Applied Physics Express* 13 (2020). DOI: `https://doi.org/10.35848/1882-0786/ab7cf0`.

A

Radiation and Expansion Force

Table A.1 shows the used variables for the radiation pressure and heat expansion force calculations of chapter 2.

Variable	Value
λ	$1560 * 10^{-9}$ $[m]$
Pulse duration	$100 * 10^{-15}$ $[s]$
Average Power	$100 * 10^{-3}$ $[W]$
Spot radius	$2.5 * 10^{-6}$ $[m]$
E	250 $[GPa]$
c	$300 * 10^{6}$ $[m/s]$
c_p	673 $[J/kgK]$
ρ	3170 $[kg/m^3]$
q	$0.1 * 10^{-}12$ $[J]$
α_L	$2.5 * 10^{-6}$ $[1/K]$

Table A.1: Variables for the radiation and expansion forces.

Equation (A.1) shows the radiation pressure force for a perfect reflecting surface. Here, I is the light intensity, A is the laser spot area and c is the speed of light. This results in a radiation pressure force of $66 * 10^{-}12$N.

$$F_{radiation} = \frac{2IA}{c} \tag{A.1}$$

For the heat expansion force calculation, it is assumed that the total laser pulse energy is absorbed by the material and converted to heat. First, the temperature change due to the increased energy of the absorbed light is calculated. This is done with equation (A.2) where q is the heat energy, c_p the materials specific heat property, m the mass of the heated material and ΔT the temperature change. This is followed by calculating the axial stress ϵ with equation (A.3) where α_L is the materials thermal expansion coefficient. Equation (A.4) shows the resulting force equation. Here, E is the Young's modulus and A is the laser spot area. This results in a heat expansion force of $3.75 * 10^{-7}$N.

For the mass of the material, only the volume of the spot area multiplied by the membrane thickness of $80nm$ is taken into account for comparing the forces present on the laser spot location. In reality, the heated material mass would be larger since the energy will dissipate through the material beyond the spot radius area. This will result in a lower temperature change and thus a smaller expansion force.

$$q = c_p * m * \Delta T \tag{A.2}$$

$$\epsilon = \alpha_L * \Delta T \tag{A.3}$$

$$F_{expansion} = E * \epsilon * A \tag{A.4}$$

B

Bandgap Simulations

Name	Expression	Value	Description
a	$1um$	$1E-6$[m]	Lattice Constant
R	$0.45*a$	$5E-7$[m]	Hole Radius
$fmin$	$a-2*R$	$1E-7$[m]	Minimum feature size
kx	$if(k<1, pi/a*k, if(k<2, pi/a, (3-k)*pi/a))$	-	X component of the Wave number
ky	$if(k<1, 0, if(k<2, (k-1)*pi/a, (3-k)*pi/a))$	-	Y component of the Wave number

Table B.1: Parameters Square Lattice

Name	Expression	Value	Description
a_0	$1um$	$1E-6$[m]	Lattice Constant
R	$0.45*a$	$5E-7$[m]	Hole Radius
$fmin$	$a-2*R$	$1E-7$[m]	Minimum feature size
α	$if(k<1, 2/3*(1-k), if(k<2, 0.5*(k-1), 1/6*(k+1)))$	-	-
β	$if(k<1, 1/3*(1-k), if(k<2, 0.5*(k-1), -1/6*(k-5)))$	-	-
$k0$	$(4*\pi)/(\sqrt{3}*a_0)$	-	-
kx	$alpha*k0*sqrt(3)/2$	-	X component of the Wave number
ky	$k0*(beta-0.5*alpha)$	-	Y component of the Wave number

Table B.2: Parameters Hexagonal Lattice

C

Straight Waveguide Simulations

Name	Expression	Value	Description
a	$1um$	$1E-6$[m]	Lattice Constant
R	$0.45*a$	$5E-7$[m]	Hole Radius
$fmin$	$a-2*R$	$1E-7$[m]	Minimum feature size
WWg	$a/2$	$5E-7$[m]	WG width
$Rspot$	$a/2$	$5E-7$[m]	Excitation spot radius
$WedgeWidth$	$4*a$	$4E-6$[m]	Excitation wedge width

Table C.1: Geometry Parameters for the straight WG simulations

Name	Expression	Value	Description
cs_SiN	5730 [m/s]	5730 [m/s]	Shear Wave Speed SiN
cp_SiN	9670 [m/s]	9670 [m/s]	Pressure Wave Speed SiN
$lam0\_SiN$	$cs\_SiN/f0$	$1.959E-6$ [m]	Wavelength in SiN
$f0$	2.925[GHz]	$2.925E9$ [Hz]	Gaussian frequency
$omega$	$2*\pi*f0$	1.837 [1/s]	Angular frequency
f_norm	$omega*a/(2*pi*cp_SiN)$	0.3025	Normalized frequency
$T0$	$1/f0$	$3.419E-10$[s]	Period
dt	$T0/10$	$3.419E-11$[s]	Time step
$time$	$5E-8$[s]	$5E-8$[s]	Simulation Time
QWL	$lam0\_SiN/4$	$4.897E-7$[m]	Quarter wave length
Amp	2	2	Amplitude

Table C.2: Physics Parameters for the straight WG simulations

D

Total Energy MATLAB Code

This code is used to calculate the total energy values for the straight WG wedge excitations. The same code setup is used to calculate the total energies for the other simulations, by changing the input tables.

```
clc
clear all
close all
%%
%Tables are in Energy density form. Need to multiply by the thickness to
%recieve the total energy in Joule
thickness = 80E-9;

%%
%Loading in the Tables
%0x3
WG0x3 = readtable('WG0x3');
Shield0x3 = readtable('Shield0x3');
%1x3
WG1x3 = readtable('WG1x3');
Shield1x3 = readtable('Shield1x3');
%2x3
WG2x3 = readtable('WG2x3');
Shield2x3 = readtable('Shield2x3');
%3x3
WG3x3 = readtable('WG3x3');
Shield3x3 = readtable('Shield3x3');
%4x3
WG4x3 = readtable('WG4x3');
Shield4x3 = readtable('Shield4x3');

%%
%Adding the energy densities of the elastic(stored) energy density and the
%kinetic energy density. For both WG and Shield domains
%0x3
WG_Energy0x3 = (WG0x3.Var2 + WG0x3.Var3)*thickness;
Shield_Energy0x3 = (Shield0x3.Var2 + Shield0x3.Var3)*thickness;
%1x3
WG_Energy1x3 = (WG1x3.Var2 + WG1x3.Var3)*thickness;
Shield_Energy1x3 = (Shield1x3.Var2 + Shield1x3.Var3)*thickness;
%2x3
WG_Energy2x3 = (WG2x3.Var2 + WG2x3.Var3)*thickness;
```

```
Shield_Energy2x3 = (Shield2x3.Var2 + Shield2x3.Var3)*thickness;
%3x3
WG_Energy3x3 = (WG3x3.Var2 + WG3x3.Var3)*thickness;
Shield_Energy3x3 = (Shield3x3.Var2 + Shield3x3.Var3)*thickness;
%4x3
WG_Energy4x3 = (WG4x3.Var2 + WG4x3.Var3)*thickness;
Shield_Energy4x3 = (Shield4x3.Var2 + Shield4x3.Var3)*thickness;

Time = WG0x3.Var1;
%%
%Calculating the ratio of the elastic energy in the WG and the Shield
%Done by the trapezoiding trapz function to calculate the area under the
%curves of the previous figures
%Performance value for the 0x3 wedge
Z1 = trapz(Time,WG_Energy0x3);
Z2 = trapz(Time,Shield_Energy0x3);
Performance0x3 = Z1/(Z1+Z2)*100;
%Performance value for the 1x3 wedge
Z3 = trapz(Time,WG_Energy1x3);
Z4 = trapz(Time,Shield_Energy1x3);
Performance1x3 = Z3/(Z3+Z4)*100;
%Performance value for the 2x3 wedge
Z5 = trapz(Time,WG_Energy2x3);
Z6 = trapz(Time,Shield_Energy2x3);
Performance2x3 = Z5/(Z5+Z6)*100;
%Performance value for the 3x3 wedge
Z7 = trapz(Time,WG_Energy3x3);
Z8 = trapz(Time,Shield_Energy3x3);
Performance3x3 = Z7/(Z7+Z8)*100;
%Performance value for the 4x3 wedge
Z9 = trapz(Time,WG_Energy4x3);
Z10 = trapz(Time,Shield_Energy4x3);
Performance4x3 = Z9/(Z9+Z10)*100;

%%
figure(1)
subplot(5,1,1)
hold on
plot(Time,WG_Energy0x3,'r-')
plot(Time,Shield_Energy0x3,'r--')
title ('0x3')
subplot(5,1,2)
hold on
plot(Time,WG_Energy1x3,'g-')
plot(Time,Shield_Energy1x3,'g--')
title ('1x3')
subplot(5,1,3)
hold on
plot(Time,WG_Energy2x3,'b-')
plot(Time,Shield_Energy2x3,'b--')
title ('2x3')
ylabel('Total Energy (J)')
subplot(5,1,4)
hold on
plot(Time,WG_Energy3x3,'m-')
plot(Time,Shield_Energy3x3,'m--')
```

```
title ('3x3')
subplot(5,1,5)
hold on
plot(Time,WG_Energy4x3,'k-')
plot(Time,Shield_Energy4x3,'k--')
title ('4x3')
xlabel('Time (seconds)')

figure(2)
hold on
plot(Time,WG_Energy4x3,'r-','LineWidth',1.5)
plot(Time,Shield_Energy4x3,'k--','LineWidth',1.5)
xlabel('Time (s)','FontSize',15);
ylabel('Total Energy (J)','FontSize',15);
```

E

FFT MATLAB Code

This code is used to calculate the FFT values for frequencies regarding the 1st Hexagonal bandgap. The same code setup is used to calculate FFT's for other frequencies and bandgaps, by changing the input frequencies and bandgap regions.

```
clc
clear all
close all

%Script to calculate the Fourier Transform of the Gaussian pulse excitation
%wave.
%https://nl.mathworks.com/help/matlab/math/fourier-transforms.html

%2.925E9 is the 1st mid-gap frequency
%5.525E9 is the 2nd mid-gap frequency
%8.175E9 is the 3rd mid-gap frequency
f1 = 2.925E9;          %mid-gap frequency, peak is to the left of the bandgaps center region
f2 = 2.450E9;          %peak is close to the left edge of the bandgaps region
f3 = 3.250E9;          %peak is in the center of the bandgap region
f4 = 3.975E9;          %peak is close to the right edge of the bandgaps region
T1 = 1/f1;
T2 = 1/f2;
T3 = 1/f3;
T4 = 1/f4;
dt1= T1/10;
dt2= T2/10;
dt3= T3/10;
dt4= T4/10;
time1 = 1.2E-8;
time2 = 1.2E-8;
time3 = 1.2E-8;
time4 = 1.2E-8;
Amp = 2;
t1 = 0:dt1:time1-dt1;
t2 = 0:dt2:time2-dt2;
t3 = 0:dt3:time3-dt3;
t4 = 0:dt4:time4-dt4;
```

```
x1 = (Amp*sin(2*pi*f1*t1)).*(exp(-((t1-6*T1)/(2.5*T1)).^2));
x2 = (Amp*sin(2*pi*f2*t2)).*(exp(-((t2-6*T2)/(2.5*T2)).^2));
x3 = (Amp*sin(2*pi*f3*t3)).*(exp(-((t3-6*T3)/(2.5*T3)).^2));
x4 = (Amp*sin(2*pi*f4*t4)).*(exp(-((t4-6*T4)/(2.5*T4)).^2));

y1 = fft(x1);
fs1 = 1/T1;
f1 = (0:length(y1)-1)*fs1/length(y1);
y2 = fft(x2);
fs2 = 1/T2;
f2 = (0:length(y2)-1)*fs2/length(y2);
y3 = fft(x3);
fs3 = 1/T3;
f3 = (0:length(y3)-1)*fs3/length(y3);
y4 = fft(x4);
fs4 = 1/T4;
f4 = (0:length(y4)-1)*fs4/length(y4);

%%
%1st Bandgap center line
c1 = [2.925E9, 2.925E9];
c2 =  [0, 45];
%%
subplot(4,1,1)
plot(t1,x1,'r')
title ('Frequency = 2.925GHz','FontSize',15)
ylabel('Amplitude','FontSize',10)
subplot(4,1,2)
plot(t2,x2,'g')
title ('Frequency = 2.450GHz','FontSize',15)
ylabel('Amplitude','FontSize',10)
subplot(4,1,3)
plot(t3,x3,'b')
title ('Frequency = 3.250GHz','FontSize',15)
ylabel('Amplitude','FontSize',10)
subplot(4,1,4)
plot(t4,x4,'k')
title ('Frequency = 3.975GHz','FontSize',15)
xlabel('Time (s)','FontSize',15)
ylabel('Amplitude','FontSize',10)


figure(2)
hold on
plot(f1,abs(y1),'r')
plot(f2,abs(y2),'g')
plot(f3,abs(y3),'b')
plot(f4,abs(y4),'k')
b1 = area([2.1E9 3.75E9], [45 45]);
plot(c1,c2,'k');
b1.FaceAlpha = 0.1;
b1.FaceColor = [1 0 0];
xlabel('Frequency (Hz)','FontSize',15)
ylabel('Magnitude','FontSize',10)
title('FFT Gaussian Pulses','FontSize',10)
```

F

Splitter Simulations

Name	Expression	Value	Description
a	$1um$	$1E-6$[m]	Lattice Constant
R	$0.45*a$	$5E-7$[m]	Hole Radius
$fmin$	$a-2*R$	$1E-7$[m]	Minimum feature size
WWg	$a/2$	$5E-7$[m]	WG width
$WedgeWidth$	$4*a$	$4E-6$[m]	Excitation wedge width
$a2$	$sqrt((2*R+WWg)^2-(R+(WWg/2))^2)$	$1.21E-6$[m]	Variable used to locate WG2

Table F.1: Geometry parameters for the splitter simulations

Name	Expression	Value	Description
cs_SiN	5730 [m/s]	5730 [m/s]	Shear Wave Speed SiN
cp_SiN	9670 [m/s]	9670 [m/s]	Pressure Wave Speed SiN
$lam0\_SiN$	$cs\_SiN/f0$	$1.959E-6$ [m]	Wavelength in SiN
$f0$	2.925[GHz]	$2.925E9$ [Hz]	Gaussian frequency
$omega$	$2*\pi*f0$	1.837 [1/s]	Angular frequency
f_norm	$omega*a/(2*pi*cp\_SiN)$	0.3025	Normalized frequency
$T0$	$1/f0$	$3.419E-10$[s]	Period
dt	$T0/10$	$3.419E-11$[s]	Time step
$time$	$5E-8$[s]	$5E-8$[s]	Simulation Time
QWL	$lam0\_SiN/4$	$4.897E-7$[m]	Quarter wave length
Amp	2	2	Amplitude

Table F.2: Physics parameters for the splitter simulations

G
Straight WG Designs

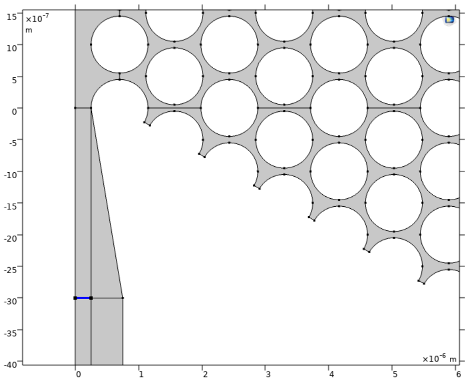

(a)

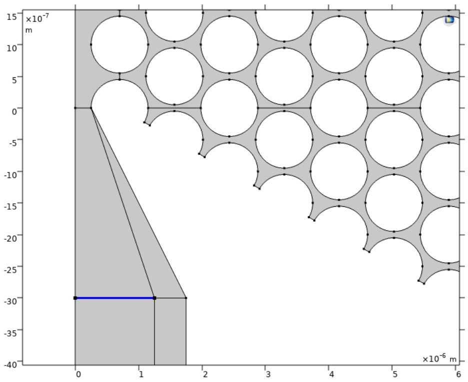

(b)

Figure G.1: (a)design with wedge shape 0x3. (b)design with wedge shape 1x3

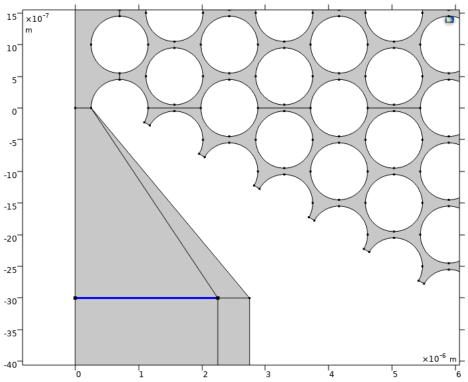

(a)

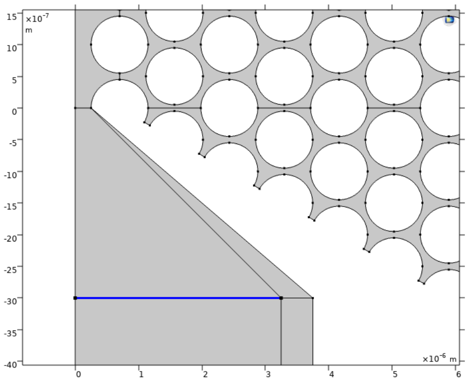

(b)

Figure G.2: (a)design with wedge shape 2x3. (b)design with wedge shape 3x3

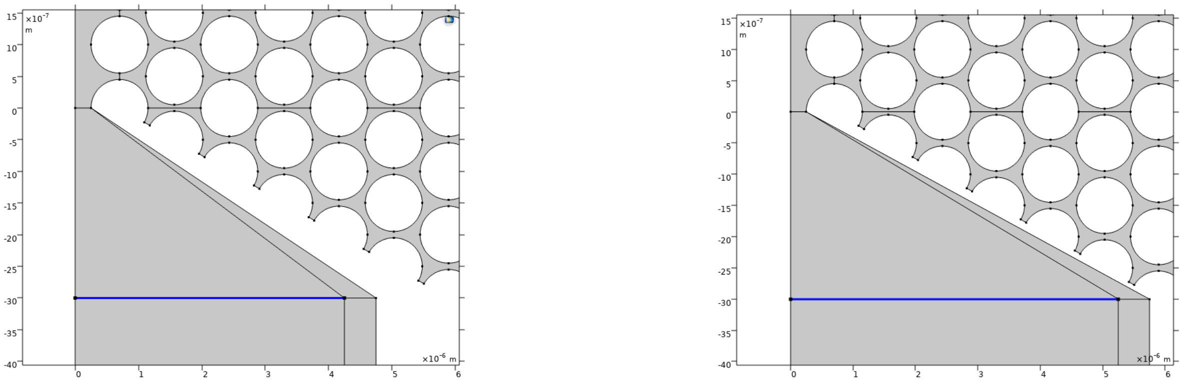

(a) **(b)**

Figure G.3: (a)design with wedge shape 4x3. (b)design with wedge shape 5x3

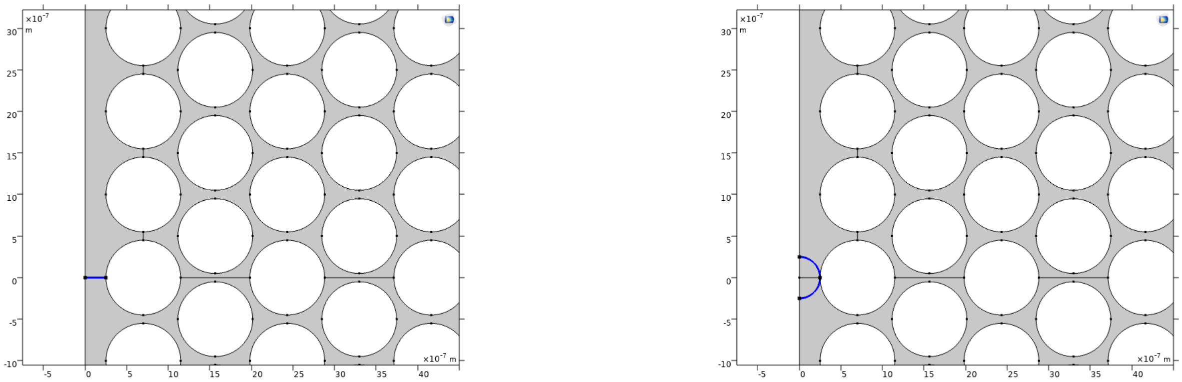

(a) **(b)**

Figure G.4: (a) spot simulation with a plane wave excitation inside the WG. (b) spot simulations with a circular spot at (0, 0).

H

Splitter Designs

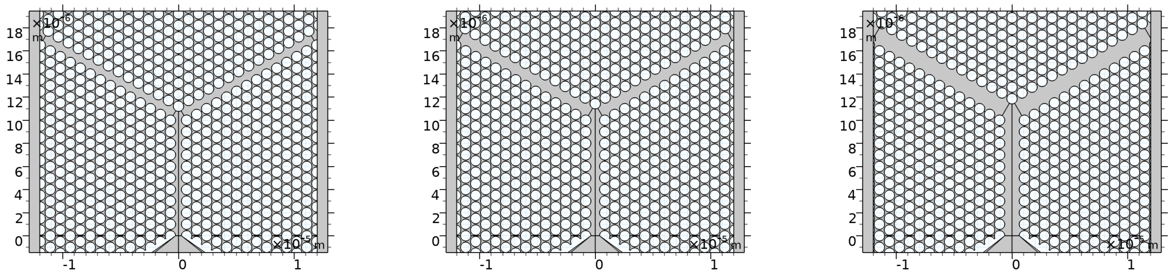

(a) (b) (c)

Figure H.1: Hexagonal splitter designs. (a) WG width 0.50a. (b) WG width 0.75a. (c) WG width 1.25a.

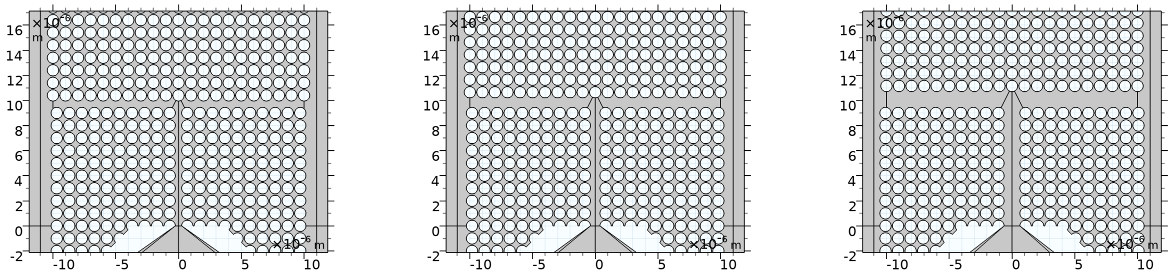

(a) (b) (c)

Figure H.2: Square splitter designs. (a) WG width 0.50a. (b) WG width 0.75a. (c) WG width 1.25a.